



This is a non-peer-reviewed preprint submitted to *EarthArXiv*

Corresponding author: Duo Li (d.li@gns.cri.nz)

The role of thermal pressurization in driving deep fault slip during the 2021 Mw8.2 Chignik, Alaska megathrust earthquake

Duo Li^{1,2}, Bo Li³, Alice-Agnes Gabriel^{4,1}, Thomas Ulrich¹, Shihao Yuan^{5,6},
Kang Wang⁹, Roland Bürgmann⁸

¹Department of Earth and Environmental Sciences, Ludwig-Maximilians-University München, Germany

²Earth Sciences New Zealand, Lower Hutt, New Zealand

³Physical Science and Engineering Division, King Abdullah University of Science and Technology,
Thuwal, Saudi Arabia

⁴Scripps Institution of Oceanography, UC San Diego, La Jolla, USA

⁵Department of Geophysics, Colorado School of Mines, Golden, USA

⁶School of Geography, Environment and Earth Sciences, Victoria University of Wellington, NZ

⁷Department of Geophysics, Colorado School of Mines, Golden, USA.

⁹EarthScope Consortium Inc., Washington DC, USA

⁸Department of Earth and Planetary Science and Berkeley Seismology Lab, University of California,
Berkeley, USA

Key Points:

- A 3D dynamic rupture model reproduces key kinematic source characteristics of the Chignik earthquake inferred from joint inversions
- Thermal pressurization of pore fluids controlled by variable shear zone properties influences deep ruptures on subduction faults
- Along-strike variations in shear zone properties may substantially influence megathrust rupture behavior and long-term slip budget

Corresponding author: D. Li, d.li@gns.cri.nz

Abstract

The 2021 M_w 8.2 Chignik earthquake ruptured a weakly coupled portion of the deep slab in the eastern Aleutian-Alaska subduction zone, with no significant shallow slip. The underlying physics driving such large earthquakes nucleating at large depth and their impact on seismic and tsunami hazards remain poorly understood. We perform 3D dynamic rupture simulations that couple thermal pressurization of pore fluids within a finite shear zone with geodetically derived slip deficit models, unraveling the potential mechanisms governing deep coseismic ruptures in a fluid-rich subduction environment. Our simulations account for 3D slab geometry, regional subsurface material properties, fault slip deficit models, fast velocity-weakening rate-and-state friction, and thermally activated weakening mechanisms. Array- and frequency-dependent back-projection analyses validate the key kinematic source characteristics in the preferred model, highlighting the role of fault shear zone heterogeneities in rupture initiation, propagation, and arrest. Our results reveal a smoothly expanding rupture, which initiates on the deep slab close to the brittle-ductile transition and dynamically propagates across multiple locked asperities, driven by rising temperature and pore fluids at increasing slip rates. Our study demonstrates that the enhanced weakening resulting from thermal pressurization of pore fluid could promote the rupture of a large, partially locked region of the fault interface. We find that along-strike variations in pore fluid evolution, frictional properties and long-term slip deficit patterns collectively influence rupture dynamics and its termination at shallower depths. These data-integrated models provide insight into the mechanical conditions in the Semidi gap with important implications for regional seismic and tsunami hazards.

Plain Language Summary

The 2021 M_w 8.2 Chignik earthquake has ruptured a deep portion of the fault with minimal shallow slip in the eastern Aleutian-Alaska subduction zone. We use physics-based, data-integrated numerical modeling and back-projection analyses to investigate how such a large earthquake starts and propagates along the deeper parts of faults. We employ back-projection analyses, which identifies where and when seismic energy was radiated during an earthquake by stacking waveforms recorded at seismic arrays, to reveal phases of acceleration and deceleration at the rupture propagated towards the eastern end. Our preferred model shows that rising temperature and pore fluid pressure, triggered by rapid fault slip, drive a deep rupture consistent with key features reported in previous studies. Tsunami sim-

ulations based on this model align with the relatively small wave amplitudes recorded at coastal tide gauges. Our model demonstrates that fault-shear-zone structural complexities and variations play a critical role in controlling how the earthquake begins, grows, and stops. Our study also raises important questions about the mechanical conditions and tsunami hazards associated with the shallower subduction interface in the Semidi gap.

1 Introduction

The Aleutian-Alaska subduction zone marks the convergent plate boundary between the Pacific and North American plates. In history, several significant megathrust earthquakes have occurred along this trench, including the 1964 $M_{9.2}$ Prince William Sound earthquake, which ruptured a 640 km-long segment of the plate interface and caused severe tsunami hazards around the Pacific Ocean (Ichinose et al., 2007; von Huene et al., 2012). On July 29, 2021, a M_w 8.2 megathrust earthquake, known as the Chignik earthquake, struck off-shore of the Alaska Peninsula. It initiated near the western edge of the Semidi segment (Elliott et al., 2022; Ye et al., 2022), which most recently ruptured in the 1938 M_w 8.3 event (C. Liu et al., 2022). While the 1938 Semidi event has primarily ruptured the shallower subduction interface near the trench, as indicated by aftershock locations (Davies et al., 1981; Ye et al., 2022) and tsunami wave modeling (Freymueller et al., 2021), the 2021 Chignik earthquake occurred on the relatively deeper fault, similar to the 2020 $M_{7.8}$ Simeonof Island event, which ruptured the deeper portion of the adjoining Shumagin gap (Herman & Furlong, 2021; Ye et al., 2021; Xiao et al., 2021) (Figure 1). The Chignik rupture stopped in the east before reaching the rupture area of the 1964 $M_{9.2}$ event (Elliott et al., 2022), raising questions about the potential seismic and tsunami risk of the shallower fault sections that remained unruptured (Mulia et al., 2022; Brooks et al., 2023).

The spatio-temporal distribution of subduction earthquakes in the eastern Aleutian-Alaska trench could be related to tectonic or structural asperities (von Huene et al., 2012; Zhao et al., 2022), sedimentary fluid variation (J. Li et al., 2018; Wang et al., 2024; Z. Li et al., 2024a), lithospheric rheology (Eberhart-Phillips et al., 2006; Arnulf et al., 2022) and geodetic-constrained fault segmentation (S. Li et al., 2016; Drooff & Freymueller, 2021; Xiao et al., 2021). Geodetically-constrained interseismic fault slip deficit models inferred using land-based GNSS networks reveal relatively strong contrasts that may correlate with the rupture segmentation of historical earthquakes (Drooff & Freymueller, 2021). Imaging of these strong changes in interseismic fault coupling (S. Li et al., 2016; Drooff & Freymueller, 2021)

could reveal the along-strike variations in pore fluid contents (Wang et al., 2024) influenced by the nature and amount of subducting sedimentary material (J. Li et al., 2018). A strongly-coupled area to the east of the Semidi segment is consistent with the rupture area of the 1964 Prince William Sound earthquake, indicating a strongly-locked fault capable of hosting disastrous tsunamigenic earthquakes (Drooff & Freymueller, 2021; Wang et al., 2024). However, due to the limited number of off-shore stations, interseismic fault coupling models in this region typically assume an ad-hoc simple functional decrease of coupling coefficient along down-dip distance (Drooff & Freymueller, 2021; Xiao et al., 2021). This limitation probably explains why these models fail to explain the coseismic rupture on the relatively deep faults of the 2020 M7.6 and M7.8 event pair and the 2021 M8.2 Chignik event.

Complementing kinematic models with assumed depth-dependent coupling variation, Zhao et al. (2022) proposed a new fault coupling model based on the assumption of persistent rupture asperities on the subducting slab, which shows good agreement with both interseismic and postseismic signals in the local GPS network. However, due to the limited off-shore observations, these fault slip deficit models from land-based stations have poor resolution for off-shore deformation, which hinders a full understanding of the dynamics of large coseismic rupture (Zhao et al., 2022). Methods to assess the timing, magnitude, and spatial extents of future earthquakes using the distribution of interseismic fault locking are being explored (Kaneko et al., 2010; Yang et al., 2019). However, their outcomes remain debated because of the poorly constrained frictional properties, including potential weakening mechanisms on subduction faults. Specifically, experimental and geological evidence of thermal pressurization, which accelerates fault weakening process (Noda & Lapusta, 2013; Hirono et al., 2016; Dunham et al., 2011), has been found on exhumed subduction thrust (Ujiie et al., 2010) and proposed as a key ingredient towards more realistic scenarios. Therefore, the mechanical viability of such a weakening mechanism on subduction faults, as well as that of geodetically-constrained interseismic models in interpreting earthquake dynamics, needs confirmation through physics-based forward rupture modeling.

In this study, we investigate the nature of the Chignik earthquake rupture using a suite of physics-based, observation-driven forward models. Our 3D dynamic rupture models integrate complex fault geometry, topo-bathymetric surface, and regional velocity structure. We assume a non-Andersonian stress field promoting reverse-faulting on the shallow dipping subduction interface, constrained by stress inversion, the Mohr-Coulomb theory of frictional failure and an interseismic fault coupling model that incorporates knowledge of the

location of historical ruptures (Zhao et al., 2022). We model the nucleation, spontaneous evolution and termination of the rupture across the fault. Fault sliding is jointly determined by a combination of factors, including laboratory-derived constitutive friction incorporating dramatic weakening at high slip velocity, as well as thermally-activated pore fluid pressurization in natural fault zones. Our observationally-driven preferred scenario captures key rupture characteristics and quantitatively reproduces the main features of geodetic and seismic observations. The rupture process is consistent with back-projection analysis using multiple teleseismic arrays. We analyze different rupture phases by the effect of thermally-driven slab pore fluid pressurization and fault zone heterogeneity. Our study demonstrates that the enhanced weakening resulting from thermal pressurization of pore fluid could promote the rupture of a large, partially locked region of the fault interface. Our dynamic rupture model provides a time-dependent source of surface displacements for high-resolution tsunami wave modeling, which can in turn contribute to additional constraints for shallow coseismic slip. More generally, our simulations shed light on faulting mechanisms in fluid-bearing environments, such as in sedimentary layers and reservoirs.

2 Methods and Data

2.1 Model setup

We incorporate the 3D geometry of the subducting slab and the regional topography and bathymetry in the model domain (Figure 2a). We constrain the subduction interface by interpolating and smoothing the 5 km-sampled Slab2 model (Hayes et al., 2018) along the eastern Aleutian-Alaska margin. The slab interface is truncated to 290 km along strike to fully cover the coseismic rupture area. The shallow edge of the fault is located along the -10 km depth contour and extends horizontally from (159.8°W, 54.2°N) to (155.5°W, 55.5°N). Topography and bathymetry data from GEBCO (<https://www.gebco.net/>), originally sampled at 30 arc seconds, are resampled to a 1000 m grid size. The entire domain is then discretized into an unstructured mesh of four-node linear tetrahedral elements. The mesh is refined near the fault surface, ensuring element edge lengths no larger than 400 m. This resolution is sufficient for the minimum and median dynamic cohesive zone (Wollherr et al., 2019), estimated at 0.14 and 4.89 km, respectively, for the preferred model (Section 2.6). To improve computational efficiency, the mesh is coarsened as a function of distance to the fault surface at a rate of 0.3, gradually reducing the resolution for outgoing seismic waves while maintaining accuracy near the rupture zone.

We use the open-source software *SeisSol* (<https://github.com/SeisSol/SeisSol>) to solve the coupled dynamic rupture and wave propagation problem. *SeisSol* is based on the Arbitrary high-order accurate DERivative Discontinuous Galerkin method (ADER-DG) (Dumbser & Käser, 2006; Käser & Dumbser, 2006) and employs fully adaptive, unstructured tetrahedral meshes to combine geometrically complex 3D geological structures, nonlinear rheology, and high-order accurate propagation of seismic waves (Pelties et al., 2014; Wollherr et al., 2019; Ulrich et al., 2019; Taufiqurrahman et al., 2023). To optimize performance on modern computing architectures, *SeisSol* implements an efficient local time-stepping algorithm (Breuer et al., 2016; Heinecke et al., 2014; Uphoff et al., 2017). It has been validated against several community benchmarks following the SCEC/USGS Dynamic Rupture Code Verification exercises (Harris et al., 2009, 2018).

To prevent spurious reflected waves at the domain boundaries, the full model domain is extended to $1050 \text{ km} \times 1000 \text{ km} \times 290 \text{ km}$, which is larger than the region of interest. The computational mesh contains approximately 25 million elements. Simulating fault rupture and seismic wave propagation for a simulation duration of 140 s after the forced nucleation with basis functions of maximum polynomial order $P=3$ requires approximately 4 hours on 4,800 Skylake cores of the SuperMUC-NG supercomputer at the Leibniz Supercomputing Center (LRZ) in Germany.

2.2 Initial fault stresses

We apply a non-Andersonian stress field aligned with the reverse-faulting on the shallow-dipping subduction interface and consistent with stress orientation near subduction interfaces in a global investigation (Hardebeck, 2015). We obtain the principal stress orientation that optimally loads the nodal planes corresponding to the USGS focal mechanism (i.e. strike= 239° , dip= 14° , rake= 95°). The resulting stress tensor (b_{ij}) has its maximum principal stress σ_1 trending to N 51.1° W and plunging at an angle of 58.9° . We assume a uniform stress orientation throughout the simulation domain, even though, in reality, spatial variations might be expected along the fault (Ulrich et al., 2022; Wollherr et al., 2019).

While we use a rate-and-state friction law (Sec. 2.5) during the dynamic rupture simulations, our initial stress conditions are set in a static sense (Ulrich et al., 2019; Palgunadi et al., 2020). In this context, a fault is prone to rupture depending on its closeness to the failure threshold based on the Mohr-Coulomb failure criterion (Griffiths, 1990). Our key

constraint on the initial stress is parameterized based on the relative prestress ratio R , the ratio of the maximum potential stress drop ($\tau_0 - \tau_f$) over fault breakdown strength drop ($\sigma(\mu_s - \mu_d)$) (Aochi & Madariaga, 2003; Ulrich et al., 2019):

$$R = \frac{\tau_0 - \sigma_n \mu_d}{\sigma_n (\mu_s - \mu_d)} \quad (1)$$

where τ_0 , σ_n , μ_s , and μ_d are initial shear stress, effective normal stress, and static and dynamic friction coefficient, respectively. The static and dynamic friction coefficients used here are set to be 0.6 and 0.1, respectively, consistent with f_0 in the rate-and-state friction and f_w in the enhanced velocity-weakening in Section 2.4

We constrain the maximum value of prestress ratio on an optimally orientated fault, R_0 , using a published geodetically-inferred fault deficit model. We use the fault deficit model of Zhao et al. (2022) (referred as 'Zhao2022'), incorporating both long-term interseismic geodetic records and the effect of the stress-driven postseismic afterslip following the 2020 and 2021 earthquakes in the Alaska subduction zone, in our reference dynamic rupture scenario. This model reflects the frictional heterogeneity and thus can better explain the slip behaviors of persistent asperities on the subduction thrusts. To enhance the resolution, we resample the original fault locking coefficients between 0 and 1 onto our fault domain using a finer grid spacing.

In addition to the preferred model, we present an alternative model based on the fault slip deficit model of Drooff and Freymueller (Drooff & Freymueller, 2021), which assumes a simple linear decrease of fault coupling from the trench to the downdip to cope with the absence of trench-normal observations (Fig. S2 and Section 4.2).

The stress tensor b_{ij} is attributed to the earthquake focal mechanism, assuming an optimally-oriented nodal plane, the prestress ratio R , and the stress shape ratio ν , which is defined as $\frac{S_1 - S_2}{S_1 - S_3}$, balancing the relative amplitude of three principal stresses (i.e. $S_1 < S_2 < S_3$ where compression is negative). Here we assume $\nu = 0.5$ to promote reverse rupture for the entire fault.

The effective confining stress distribution is jointly defined by the depth-dependent lithostatic loading (σ_c) and the ratio of pore fluid pressure (λ). The lithostatic stress increases linearly with depth below sea level. The lithostatic pressure σ_c at depth z follows:

$$\sigma_c = \int_0^z \rho(z_i) g z_i \delta z_i \quad (2)$$

In practice, the effective confining stress (compression is negative), defined as $\sigma'_c = \sigma_c - P_f = (1-\lambda)\sigma_c$, with P_f the pore fluid pressure and $\lambda = \frac{P_f}{\sigma_c}$ the pore fluid pressure ratio, which is defined either depth-dependent or constant. The profile of σ_c and σ'_c is shown in Figure 2. In the latter case, it follows exactly the lithostatic gradient. Here we consider an intermediate case, in which λ increases with depth from 0.9 to 0.95, acknowledging the observed slowly increasing trend of Vp/Vs ratio along the downdip distance in seismic imaging (J. Li et al., 2018).

We also present an alternative model with constant λ in supplementary Figure S7, demonstrating the effect of varying pore fluid pressure on the coseismic rupture and dynamics.

We note that this scenario assuming a constant $\lambda = 0.9$ along the depth results in a slight larger magnitude, of M_w 8.17, attributed to the increased effective confining stress at depths

We assume a depth-dependent brittle-ductile transition should reduce the deviatoric stresses below the locked fault region. Here we use a depth-dependent stress shape function $\Omega(z)$ to gradually reduce the deviatoric stresses (Ulrich et al., 2019). The assumed seismogenic depth is inferred to be 33 km from kinematic source models.

We define function $\Omega(z)$ varying with depth as :

$$\Omega(z) = \begin{cases} 1.0 - (z_{top} - z)/(z_{top} - z_{bot}); & (z_{top} < z \leq z_{bot}) \\ 1.0 & (z \leq z_{top}) \\ 0.0 & (z < z_{bot}) \end{cases} \quad (3)$$

where z_{top} and z_{bot} is - 33 km and -37 km, respectively.

The resultant stress tensor (s_{ij}) is then determined by $\Omega(z)$, stress tensor b_{ij} derived from background stress field, and lithostatic stress σ_c following the study of Ulrich et al. (2019):

$$s_{ij}(z) = \Omega(z)b_{ij} + (1 - \Omega(z))\sigma_c(z)\delta_{ij} \quad (4)$$

2.3 Rupture nucleation

We nucleate the rupture by smoothly overstressing in both space and time within a sphere around the selected hypocenter (Harris et al., 2009). The assumed hypocenter at coordinates (158.088°W, 55.364°N) is about 10 km away from the one inferred by USGS (USGS, Last accessed: 14.10.2024b).

The additional absolute shear stress follows:

$$\sigma_{ij}^{nuc} = \sigma_{ij}^{nuc} \cdot \begin{cases} \exp(-\frac{0.5r^2}{r_d^2}), & (t \leq t_s) \\ 0, & (else) \end{cases} \quad (5)$$

where $t_s = 5.0$ s and $r_d = 2500.0$ m. r is the distance from the selected hypocenter, defined as $r = \sqrt{(x - x_0)^2 + (y - y_0)^2 + (z - z_0)^2}$. We used code WGS84UTM Mercator 11S for projecting Cartesian coordinates. σ_{ij} denotes the component of the stress decomposition using the principal stress tensor described in Methods ($\sigma_{xx} = -97.2$ MPa, $\sigma_{yy} = -122.2$ MPa, $\sigma_{zz} = -0.9$ MPa, $\sigma_{xy} = 34.7$ MPa, $\sigma_{xz} = 27.3$ MPa, $\sigma_{yz} = -35.2$ MPa). The peak shear stress increase ($\Delta\tau^{nuc}$) is 36 MPa in center of the sphere.

We note the projection of the USGS epicenter onto the Slab2 model (Hayes et al., 2018) is at 25 km depth, much shallower than the depth of 32 km of the USGS hypocenter. This inconsistency in slab depth has been discussed in the study of joint inversion (Ye et al., 2022). The lateral shift of hypocentral nucleation accommodates the shallower slab depth in Slab2. The assumed hypocenter allows capturing the early moment rate release inferred by joint seismic and geodetic inversions (Elliott et al., 2022). When locating the hypocenter at the projection of the USGS epicenter onto Slab2 model, we obtain a scenario that releases moment too fast in the first 10 s and, therefore, shorter duration compared to that of the preferred model (Figure S4). The more rapid rupture initiation translates into earlier arrival times at all GNSS stations, especially at station AC13.

2.4 Thermal pressurization of pore fluids in the fault zone

The effect of thermal pressurization (TP) has been observed in laboratory experiments for rapidly dynamic weakening under coseismic shear heating (Rice, 2006; Noda et al., 2009) and inferred as a ubiquitous weakening mechanism on statically strong natural faults (Viesca & Garagash, 2015; Noda & Lapusta, 2013). We account for thermal pressurization effects

in the fault shear zone using a set of partial differential equations that simulate the 1D diffusion of temperature (T) and pore fluid pressure (P_f) in the direction normal to the fault surface (Noda et al., 2009; Noda & Lapusta, 2013; Vyas et al., 2023). These non-linear equations account for the conservation of energy and fluid mass, Fourier’s law of heat conduction, and Darcy’s law, while neglecting advection (Rice, 2006; Rempel & Rice, 2006; Noda et al., 2009).

$$\frac{\partial T}{\partial t} = \alpha_{th} \frac{\partial^2 T}{\partial d_z^2} + \frac{\tau V}{\rho c w \sqrt{2\pi}} \exp\left(-\frac{d_z^2}{2w^2}\right) \quad (6)$$

$$\frac{\partial P_f}{\partial t} = \alpha_{hy} \frac{\partial^2 P_f}{\partial d_z^2} + \Lambda \frac{\partial T}{\partial t} \quad (7)$$

where T, P_f, τ_y, V denote the physical variables of temperature and fluid pressure in the fault shear zone, shear yield strength and slip velocity, respectively. d_z denotes the distance normal to the fault. Key fault zone hydrothermal parameters include hydraulic conductivity α_{hy} , specific heat capacity ρc , the pore pressure change per unit temperature change under undrained conditions Λ , thermal conductivity α_{th} and the half-width of fault shear zone w (Noda et al., 2009).

The possible ranges of the thermal pressurization parameters, which reflect rock inherent properties that are sensitive to tectonic environment (Vosteen & Schellschmidt, 2003), have been intensively discussed in both theoretical and experimental studies (Rice, 2006; Noda & Lapusta, 2010, 2013; Rempel & Rice, 2006) for both crustal and subduction faults. The measurement of hydraulic diffusivity for natural fault zone have been explored in the study of Wibberley (2002). We here assume $10^{-8} \sim 10^{-4} m^2/s$ for the range of hydraulic diffusivity and $0.035 \sim 0.1$ m for half width of fault shear zone. To simplify the model setup, we here relate the spatial distribution of hydraulic diffusivity to the inferred along-strike segmentation of the coseismic rupture of the 1938 Semidi earthquake (Zone C in Figure 2). We set up the three zones with different combinations of hydraulic conductivity and half-width of shear zone, representing the spatial variations in porous structure and permeability of the oceanic sedimentary layer that is reflected in seismic imaging and slip behavior (J. Li et al., 2018; Kirkpatrick et al., 2020; Guo et al., 2021; Z. Li et al., 2024b). We also

shift the boundary between zones A and C based on several trial-and-error simulations, aiming at best matching seismic and geodetic observations. Zone B is a transition between zones A and C where the critical distance is small whereas temperature and pore fluid pressure changes are reduced, matching the along-strike rupture extent. The physical parameters of the Semidi and Shumagin segments can be found in Table 1.

Specifically, we find that a segmented distribution of thermal conductivity and half-width of shear zone is required to match those observations. For example, a decrease of thermal conductivity (α_{th}) and an increase of half-width of fault shear zone (w) towards the eastern modeled fault end allow a continuous and smooth moment rate release with time and spontaneous rupture arrest before reaching the inferred shallower rupture area of the 1938 Mw 8.3 earthquake area (Freymueller et al., 2021). In addition, this variation of fault zone properties also aligns with the observed variation of beam power peaks, which are indicative of relative high-frequency energy radiation in back-projection analysis (Session 3.1; Figure 6). Key parameters of thermal pressurization adopted in the models are listed in Table 1.

In our models, the influence of thermal pressurization is crucial in maintaining spontaneous dynamic rupture following the forced nucleation. Interestingly, the imposed overstress at 35 km depth triggers a substantial temperature rise of approximately 175 K. This temperature increase, in turn, leads to a significant elevation of 20 MPa in pore fluid pressure. A more detailed discussion of the effects of TP parameters on the nucleation and dynamic rupture can be found in Section 4.4.

2.5 Rate-and-state friction with enhanced velocity-weakening on the fault

We adopt the regularized formulation of laboratory-derived rate-and-state friction (RSF) with enhanced velocity-weakening following Dunham et al. (2011) to constrain the strength of the fault. This modified formulation incorporates the effect of fast velocity-weakening observed in laboratory sliding experiments (Di Toro et al., 2011) and has been verified in the Southern California Earthquake Center community benchmark (i.g. example TPV104) (Harris et al., 2018). Theoretically, this fast-weakening effect can significantly affect the earthquake rupture process, as suggested by numerical simulations (Rice, 2006; Dunham et al., 2011).

The steady-state friction coefficient is defined as:

$$f_{ss} = f_0 + \frac{f_{LV} - f_w}{(1 + (\frac{V}{V_w})^n)^{1/n}} \quad (8)$$

with slip velocity (V), weakening velocity (V_w), fully weakened friction coefficient (f_w), and low-velocity friction coefficient (f_{LV}), which evolves as follows:

$$f_{LV}(v) = f_0 - (b - a) \ln(V/V_0) \quad (9)$$

Here, a is the direct-effect parameter, b is the state-evolution parameter, and f_0 and V_0 are the reference friction coefficient and slip velocity, respectively, the same as in RSF. In this formulation, f_{ss} approaches f_{LV} when $V \ll V_w$ and f_w when $V \gg V_w$. Laboratory experiments suggest that fast velocity weakening takes place at high slip rate ($V_w \sim 0.1$ m/s) and results in low dynamic friction coefficient ($f_w \sim 0.2$ – 0.4) (Di Toro et al., 2011). We choose $n = 8$, ensuring a numerical smooth transition to fast weakening (Dunham et al., 2011).

The effective friction coefficient f , depending on both the fault slip rate V and the state variable Θ , is regularized as:

$$f = a \sinh^{-1} \left[\frac{V}{2V_0} \exp\left(\frac{\Theta}{a}\right) \right], \quad (10)$$

The state variable Θ evolves with time following:

$$\frac{d\Theta}{dt} = -\frac{V}{D_{rs}} (\Theta - \Theta_{ss}) \quad (11)$$

where D_{rs} is the characteristic slip distance over which Θ evolves in response to velocity steps and Θ_{ss} is the value of the state variable at steady-state given by:

$$\Theta_{ss} = a \ln \left(\frac{V}{2V_0} \sinh \frac{f_{ss}(V)}{a} \right) \quad (12)$$

The characteristic state evolution distance, D_{rs} , is crucial for frictional sliding in experiments (Dieterich, 1979; Ruina, 1983) but not well constrained from seismological observations for natural faults (Day et al., 2005; Jiang et al., 2022). A carefully chosen D_{rs} could ensure both physical behavior, analogous to slip-stress behavior controlled by critical slip distance D_c in linear slip-weakening friction (Weng & Yang, 2018), and numerical conver-

gence. Estimates of D_c range from 10^{-6} m in laboratory experiments to 1-10 m from seismological observations (Scholz, 1998; Kaneko et al., 2017). Seismic inversions using near-field dense networks show that critical slip distance is physically related to fracture energy or breakdown work consumed during the crack generation and may scale with the final fault slip (Tinti et al., 2005; Gallovic et al., 2019). This seismologically-inferred scaling of D_c with the final slip or earthquake size might reflect multiple processes occurring at different scales (Cocco et al., 2023). Relatively large values of D_c , e.g. 1-3 m, are typically used for numerical modeling larger fault slips, for example, M_w 9.0+ event (Galvez et al., 2014; Ulrich et al., 2022).

We set D_{rs} to be uniformly 0.12 m and 0.8 m within Zone A and B, respectively, roughly separating the rupture areas of 1938 and 2021 events (Figure 2b). Our preferred choice of the spatial extent of Zone A, a simple combination of two circular patches, is based on a few trial-and-error simulations (Section 4.4). We find that the distribution of D_{rs} significantly affects the arrest of rupture spontaneously towards the eastern edge, after about 100 km propagation along the fault. The local increase of D_{rs} might reflect the variation of fracture energy associated with the specific fault zone properties within the eastern Kiosk segment, which was the site of the 1964 M9.2 Prince William Sound event.

The physical parameters are presented in Table 1. We further present three alternative models with different representative distributions of D_{rs} , described in Section 4.4

2.6 Assessing numerical resolution

Numerical rupture simulation must have suitable discretization resolution to capture the cohesive zone, the region behind the rupture front where stresses drop from their static to their dynamic levels (Day, 1982). The dynamic cohesive zone is highly sensitive to the stress evolution and complex weakening mechanism (Day et al., 2005). Here, we estimate the cohesive processing zone which is defined as $\Lambda_d = (T_{ds} - T_{rup})V_r$ following the approach in Wollherr et al. (2019). The 5th and 50th percentiles of the entire fault is 1.72 and 4.89 km, respectively. Our on-fault mesh size samples 4.35 and 12.1 elements within the estimated cohesive zone, respectively.

2.7 Back-projection Analysis

We analyze the details of the coseismic rupture process using the back-projection algorithm with global seismic arrays. The back-projection method uses the curvature of the wavefronts recorded at large-aperture, dense seismic arrays, and the time reversal property of these coherent waves, to determine the time and location of high-frequency seismic radiation sources (Ishii et al., 2005; Kiser & Ishii, 2017). It forms a signal beam to image the rupture process in sliding time windows. Due to its computational efficiency, back-projection has now become an important practice in earthquake science for many large and moderate earthquakes (B. Li & Ghosh, 2017; Mai et al., 2023; Xu et al., 2023; Suhendi et al., 2025).

In this study, we use three global arrays Austria Array (AU), Japan Array (JP), and European Array (EU) to track the rupture process of the Mw8.2 Chignik earthquake (Figure ??). The target region is bounded as a box from 53.5°N to 56.5°N in latitude, and 154.5°W to 159.5°W in longitude, with 0.05° and 0.025° grid spacing in longitude and latitude, respectively. Only stations with higher signal-to-noise ratios (SNR) and high across-array coherence are selected to minimize interferences from noisy signals. We apply a cross-correlation (CC) method on the 25 s time window around the direct P phase to determine waveform coherency. To balance the computation cost and the azimuth coverage of each array, we set the average CC threshold as 0.5, 0.6, and 0.8 for the AU, JP and EU Array stations, respectively. Filtering the seismograms in the frequency range between 0.1 and 2 Hz results in 47, 239, and 350 stations above the threshold for the AU, JP, and EU Arrays, respectively (Figure ??). Then we use the toolkit package *TauP* (<https://www.seis.sc.edu/taup/>) and a 1-D laterally homogeneous Earth seismic velocity model, known as *Preliminary Reference Earth Model (PREM)* (Dziewonski & Anderson, 1981), to calculate the theoretical travel time from the source grid to each seismic station. In addition, we also use the time shift obtained with the peak cross-correlation (CC) coefficients of the first arrival P phase as the empirical time calibration for the 1-D velocity structure. For each array, we use a 6-s sliding time window and 0.1-s time step through the continuous data, with the event signals included, to image the coseismic rupture process.

2.8 GNSS time series

Seven GNSS stations near the cataloged hypocenter were selected (Figure 1). The original 1-Hz GPS RINEX files were from EarthScope (formerly UNAVCO) (<https://www.unavco>

.org/data/gps-gnss/gps-gnss.html) and processed using the open-source PRIDE PPP-AR software (Geng et al., 2019) with default parameters to generate 3D displacement time series at the stations. Details of the processing flow can be found in Chen et al. (2022). The scattering of positions before the earthquake suggests an uncertainty of 1-1.5 cm for the horizontal component and 2-3 cm for the vertical component.

3 Results

In this session, we present the preferred 3D dynamic rupture model, validated with source characteristics from joint inversions. We also show the rupture kinematic characteristics derived from back-projection using dense global arrays, demonstrating the complex rupture process. Additionally, we present the evolution of temperature and pore fluid pressure due to coseismic thermal pressurization in the fault damage zone.

3.1 The preferred 3D dynamic rupture scenario

We simulate dynamic rupture evolution across the modeled 290-km-long subduction fault surface for a duration of 140 s. The rupture slowly nucleates at 30 km, then propagates to the west and east for 15 s. The rupture front predominately continues eastward towards shallower depths, with increasing slip rates. It then migrates updip, with decreasing slip rates, and terminates after 85 s (Figure 3; Supporting Information Movie S1), consistent with the kinematic inference of Elliott et al. (2022).

The extent and location of the main area of fault slip (Figure 4c), east of the nucleation, are overall consistent with the kinematic inference of Elliott et al. (2022). Yet, it appears between 30 km and 40 km, slightly deeper than inferred extent (Figure 3c). Peak slip amplitude (8 m) is also larger than inferred (6 m). Updip, lower slip amplitudes of up to 2 m are modeled. Notably, the shallower eastern region of the modeled fault, underneath the Chirikof Island, hosts up to 1 m of fault slip. The modeled scenario has a final moment magnitude M_w of 8.1, in line with the USGS inference (Figure 4b). Rupture velocity, ranging between 2 km/s and 4 km/s (Figure 4c), is consistent with our back projection analysis (Figure 6; Figure S1) and that from the kinematic inversion of Elliott et al. (2022).

Our preferred rupture model reproduces the key features of the source time function inferred from joint inversions using global teleseismic and high-rate GNSS recordings (Elliott et al., 2022; Ye et al., 2022). Remarkably, it captures the gradual increase in the moment

rate release within the first 20 s following the rupture initiation driven by both forced over-stress and enhanced thermally-activated weakening mechanism (Figure 4b). The primary peak of the moment rate occurs at 20 s after rupture initiation when the rupture breaks the central part of the main slip asperity between 20 and 45 km depth. A secondary peak in the moment rate is found at 50 s after rupture initiation when the rupture front migrates towards shallower depths underneath Chirikof Island. We note that the arrival times of the secondary peak vary significantly among different kinematic models (Figure 4b), likely indicating a less well-constrained shallower slip and different data sets and inversion algorithms used in the joint inversions (Elliott et al., 2022; Ye et al., 2022).

We demonstrate the influence of fault properties on the secondary peak in the moment release rate by presenting an alternative rupture scenario designed with a different distribution of characteristic slip distance of state (D_{rs}). This results in an amplified secondary peak associated with a larger, shallower rupture area (Section 4.4. and Figure ??). However, while this amplified energy release could better match the features of the secondary peak, it leads to an overestimation of the vertical displacements observed at GNSS station AC13, on Chirikof Island (Figure ??).

We verify the preferred rupture scenario using the static and time-dependent surface displacements recorded by nearby GNSS sites (Figures 5a and b). The model captures the large horizontal and vertical displacements observed in the Alaska Peninsula, the smaller displacement amplitudes on the other islands to the west, as well as the large displacements at GNSS station AC13 on Chirikof Island, associated with the modeled slip at shallow depth there (Figure 5a). We note that Ye et al. (2022) infers a considerable slip of up to 12 m below Chirikof Island based on a joint inversion accounting for tsunami observations. This higher shallower slip is not captured in Elliott et al. (2022), which also includes regional high-rate GNSS series data. The extent of shallow slip, which is indicative of the fault frictional strength at shallower depths, remains ambiguous, as also suggested by the analysis of early postseismic displacements (Brooks et al., 2023). As noted above, the amount of slip and associated GPS displacements at station AC13 are highly sensitive to the assumed frictional heterogeneity distribution (Section 4.4). We, therefore, rely on the fit of displacements at station AC13 to constrain the shallower slip termination.

To gain insight into the kinematics of the rupture process, we compare synthetics with the displacement time series derived from continuous GNSS observations at seven stations

(Figure 5). Our model also reproduces 1 Hz GNSS time series to the first order, especially for the stations with higher signal-to-noise ratios (stations AB13, AC21, AC40 Fig.5c). The arrival times and early waveforms agree well with observations, suggesting the simulated rupture captures the kinematics of the earthquake. The vertical components, which have lower signal-to-noise ratios, are characterized in general by larger misfits, with the notable exception of station AC13.

Our preferred model exhibits an average stress drop over the entire rupture area of 5 MPa, with higher stress drops of up to 10 MPa at depths between 30 to 40 km, where peak slip is modeled (Figure 4c-d). The smaller stress drop at shallower depths is attributed to the reduced initial confining stresses and the seismic velocity structure, featuring less consolidated low-velocity material at shallower depths. Within the ruptured area, the stress release is nearly complete.

3.2 Rupture heterogeneity inferred by back-projection analysis

To better constrain the kinematic characteristics of the Chignik earthquake, we conduct a systematic back-projection imaging study and test different frequency bands and seismic arrays (B. Li et al., 2022). The back-projection results suggest the rupture primarily breaks the fault at depths between 15 and 40 km with an average rupture velocity of about 2.5 km/s (Figure 6). The rupture initiates at a location farther west than the USGS hypocenter, which aligns with our selected nucleation described in Section 2.3. The rupture spreads bilaterally and then stops to the west at about 15 s while continuing to the east until approximately 70-75 s. Between 30 s and 45 s, the rupture accelerates up to a velocity of approximately 4 km/s then decelerates (Figure S5). We observe a gradual migration of the rupture to the east at varying depths in the first ~ 50 s. Finally, the rupture migrates to shallower depths and terminates below Chirikof Island, consistent with the kinematic inference of Elliott et al. (2022) and our dynamic rupture scenario.

Our array- and frequency-dependent back-projection results suggest potentially complex rupture processes during the Chignik earthquake, likely influenced by rupture heterogeneity and directivity effects (B. Li et al., 2022). We observe several peaks in beam power potentially associated with strong radiation energy appearing around the central slip patch as well as the eastern shallow rupture region, independent of array locations and frequency bands (insets in Fig. 6d; Figure S6 and S7). We note multiple peaks arising in beam power

when the rupture front migrates updip, supporting our hypothesis of fault shear zone variations affecting the rupture process. The independent analyses are in good agreement with our dynamic rupture simulations.

3.3 Thermal pressurization during coseismic rupture

The inclusion of thermally-driven 1D pore fluid diffusion across the fault zone surface is crucial in understanding the influence of dynamic weakening in coseismic rupture on fluid-rich faults (Rempel & Rice, 2006; Noda & Lapusta, 2010, 2013). Building on previous numerical studies (Hirono et al., 2016; Vyas et al., 2023), we vary the hydraulic diffusivity α_{hy} and shear zone half-width w while keeping the other key parameters constant. Our scenario-dependent choice of α_{hy} and w results in an appropriate temperature increase ($\Delta T < 175$ K) when the fault slides at coseismic rates, elevating the pore fluid pressure, reducing the frictional strength of the fault and ensuring a slow initiation (Figure: 7). The contribution of pore fluid pressure to fault weakening is significant: pore fluid pressure increase of up to 12 MPa is modeled, corresponding to a temperature increase of up to 175 K, at a depth of 30 km on the fault (Figure 7). Due to the lower initial pre-stress, constrained by the lower level of fault coupling within the hypocenter area, our modeled rupture accumulates smaller seismic moment without a significant increase in temperature and pore fluid pressure (Figure ??).

The simulated coseismic temperature and pore fluid pressure increases are spatially heterogeneous (Figure 7a and b), and related to the assumed variations of both frictional and thermal-hydraulic parameters. We distinguish three sub-regions with distinct evolution of temperature and pore fluid pressure along the rupture path. The assumed fault-zone properties in Zone A (i.e. higher hydraulic diffusivity and smaller shear zone half-width) promote a stronger thermal pressurization effect. Combined with the low assumed characteristic slip distance of state (D_{rs}) - a frictional parameter that substantially impacts the fracture energy on the expanding fault surface - this results in higher slip rates and greater increases in temperature and pore fluid pressure (Figure 7c). Zone B and C both have relatively lower thermal pressurization potential. However, because Zone C has a larger D_{rs} , it experiences a reduction in fault slip rate and thus a smaller increase in temperature and pore fluid pressure, compared to Zone B (Figure 7d,e). The spatial patterns of temperature and pore fluid pressure reflect a complex rupture process. The peaks in temperature and pore fluid pressure increase appear between 30 and 40 km from the nucleation which

may be related to higher stress drop and stronger seismic radiation in back-projection analysis. Our models incorporating thermal pressurization of fault shear zone highlight its significant impact on the eventual rupture dynamics in our simulation.

4 Discussion

4.1 Rupture dynamic behavior and fault coupling model

Interseismic fault slip deficit models inferred from dense geodetic observations provide valuable insights into the long-term slip budget and the rupture extent of potential earthquakes. These models are expected to play a crucial role in seismic hazard assessment in the future (Kaneko et al., 2010; Yang et al., 2019; Konca et al., 2008). Numerical studies have demonstrated that interseismic fault deficit models can be used as a proxy for constraining fault stress conditions and evaluating future earthquake potential (Yang et al., 2019; Hok et al., 2011). However, the geodetically derived kinematic fault coupling is, in most cases, a highly smoothed representation of actual fault coupling conditions and may be biased by applied smoothing constraints and assumptions made to address the limited model resolution. For example, the 2011 Tohoku-Oki earthquake ruptured a portion of the subduction interface inferred as modestly coupled by inversion of geodetic data from a land-based network (Simons et al., 2011). This event highlights the large variations in model outcomes depending on the chosen regularization approach and the importance of considering such uncertainties and potential biases in assessing seismic hazards (Loveless & Meade, 2011). Under specific conditions, megathrust earthquakes can break more than one inferred firmly-locked asperity and generate more damage than expected, as observed in the 2010 M_w 8.8 Maule earthquake (Vigny et al., 2011). Understanding the mechanical conditions allowing such barrier-breaking rupture is possible using advanced numerical models (Kaneko et al., 2010; Cattania & Segall, 2021; B. Li et al., 2023; Jia et al., 2023; D. Liu et al., 2022), but requires constraining geometrical and structural heterogeneity with adequate near-source observations.

Our dynamic models show that the interseismic fault deficit model can constrain a mechanically feasible rupture, depending on factors governing the dynamic weakening mechanisms, including fault zone and frictional heterogeneity. The fault slip of our modeled event roughly focuses on the asperity indicated by the fault deficit model, in line with the conceptual models of persistent megathrust rupture asperities based on eastern Alaska sub-

duction (Zhao et al., 2022) and the global dataset of modern seismic records (Lay et al., 2012). The slip asperity that hosts the Chignik earthquake is spatially correlated with low V_p/V_s ratios revealed by seismic imaging (Wang et al., 2024), suggesting that tectonic structure is valuable for assessing seismic potentials. However, the assumed heterogeneity of fault zone properties is important in bounding the eastward rupture extent and reproducing surface deformation of the Chignik earthquake (Elliott et al., 2022). Constraining heterogeneity with various geodetic and seismological observations might broaden our understanding of the fault deformation in different stages of the earthquake cycles, including interseismic, coseismic, and postseismic (Q. Meng & Duan, 2022; Jiang et al., 2022; D. Liu et al., 2022; W. Meng et al., 2018; Ozawa et al., 2022; Romanet & Ozawa, 2021; Erickson et al., 2023).

The Chignik earthquake rupture stopped before reaching the 1964 M9.2 earthquake rupture area, posing a question on potential of future coseismic ruptures (Ye et al., 2022; Elliott et al., 2022). Brooks et al. (2023) has shown that a considerably rapid and large afterslip occurred near GNSS station AC13 on Chirikof Island, indicating continuous creeping fault deformation toward shallower depths in this region. The occurrence of afterslip and the lack of triggering of the M9.2 rupture area (i.e. Kiosk segment) may suggest either a long healing period following the M9.2 coseismic rupture or a higher static fault strength that inhibits coseismic yielding. Consequently, future research should focus on the potential earthquake hazard at depths above 25 km .

4.2 Rupture model constrained by an alternative fault deficit model

To investigate the impact of variations in interseismic fault coupling, we test an alternative initial fault stress model based on the plate deficit model of Drooff and Freymueller (Drooff & Freymueller, 2021), hereafter referred to as ‘DF2021’. This model, prescribing linear transition of coupling with distance from the trench, provides a constraint on along-strike segmentation of slab fault coupling. Since onshore stations cannot constrain the seismic coupling near the trench, assumptions of fully- or strongly-coupled faults near the trench were also made. This model gives a coupling coefficient of 0.4 at 35 km depth on the Semidi Gap. Specifically, this model shows two strong contrasts in the fault coupling coefficient between Shumagin and Semidi and between Semidi and the rupture area of the 1964 M9.2 Prince Williams Sound, respectively (Figure ??).

The prestress ratio R_0 on the optimally-oriented fault constrained by coupling coefficients from ‘DF2021’ differs notably from the preferred model, especially for depths between 30 and 40 km (Fig. 8c). To reproduce key characteristics of the earthquake with DF2021, the heterogeneous friction and hydro-thermal parameters constrained based on Zhao2022 (Zhao et al., 2022) need to be adapted.

First of all, since the prestress condition on the fault has been considerably changed in DF2021, a different distribution of characteristic slip distance of state (D_{rs}) is needed to match the observation (e.g. fault slip and magnitude). By trial-and-error, we find that choosing the maximum and minimum D_{rs} to be 1.0 and 0.2 m allows for satisfactorily capturing most key earthquake characteristics. The distribution of D_{rs} varying on the fault is shown in Figure 8.

Secondly, we increase the half shear zone width parameter w from 0.035 to 0.10 m and the hydraulic diffusivity α_{hy} from 10^{-8} to 10^{-4} m^2/s to reproduce the comparable temperature and pore fluid increase in the western fault portion as the preferred model based on Zhao2022 and the along-strike extent of the rupture inferred from joint inversion. The distribution of coseismic change in temperature and pore fluid pressure for this model is shown in Figure ??.

This alternative rupture scenario reproduces most key characteristics captured in the preferred scenario, based on Zhao2022 (Zhao et al., 2022); however, substantial differences are noted. The alternative scenario results in a moment magnitude of 8.1 and a shorter rupture duration of 50 s (Figure 8). The main peak of the moment rate release occurs 15 s earlier than inferred and overshoots the peak values by 10-20% (Figure 8b). This model yields overall comparable displacements at most GNSS stations except for station AC13, which then has a near-zero displacement (Figs. 8a). In fact, the lower stress drop in the rupture path towards the eastern shallower fault prevents rupture propagation to this location (Fig. 8a). Compared to the preferred model, this alternative model exhibits a faster initial phase within the first 10 s, a smaller second peak in the moment rate release, and a limited rupture extent (Figure 8b; Movie S3). These differences make it less consistent with observations.

4.3 Coseismic expansion and termination of rupture driven by variation in fault zone properties

We examine the influence of fault zone heterogeneity on the rupture dynamics, particularly its role in the initial expansion, propagation and termination of the rupture process. The mechanism underlying the initiation of megathrust earthquakes remains mysterious, as they occasionally occur on low-coupling portions of subduction faults (Yue et al., 2013; Simons et al., 2011) and are usually not well observed (Tape et al., 2018). The 2021 M8.2 Chignik earthquake, as well as the 2020 M7.8 and M7.6 earthquakes in the Shumagin gap, occurred at relatively deep locations, below the brittle-ductile transition, where the buildup of elastic strain energy is expected to be lower than seismogenic depths. Rather than by coseismic slip, most of the plate convergence at increasing depths is expected to be accommodated by aseismic shearing slip enabled by increasingly ductile fault-zone rheology, as observed in specific subduction zones such as Cascadia and Mexico (Gao & Wang, 2017; D. Li & Liu, 2016; Bruhat & Segall, 2016; Perez-Silva et al., 2021).

Our model demonstrates that the time-dependent evolution of temperature and pore fluid pressure governed by laboratory-derived 1D thermal pressurization plays a critical role in controlling coseismic extension at deep nucleation depth. While dilatancy-strengthening leading to the drop of pore pressure in the fault zone may play a role in stabilizing the ruptured fault and prevent it from rapid slip during fault slip, as proposed as a mechanism for slow slip (e.g. Segall et al. 1995, Liu and Rubin, 2014), we here focus on rapid weakening during coseismic slip.

We interpret the along-strike variation in hydraulic conductivity and characteristic fault shear zone thickness as the manifestation of varying properties and thickness of the sedimentary layer on top of the oceanic slab (J. Li et al., 2018). Although the role of elevated pore fluid pressure in modulating earthquake behavior has been previously proposed (Moreno et al., 2018; Madden et al., 2022), its impact on the dynamic weakening process on natural faults, particularly in fluid-rich megathrust environments, remains unclear (Hirono et al., 2016). Given the large uncertainty in thermal pressurization parameters, our choice is not unique, and other combinations of parameters might reproduce the same rupture process. The evolution of temperature and pore fluid pressure with respect to a growing slip pulse can be found at coseismic slip rate, although different amplitudes may arise with various parameter setups (Noda et al., 2009). Additionally, we test the influence of variable back-

ground pore fluid pressure on dynamic rupture. For instance, we note that a slight increase in confining stresses at depths, resulting from a lower pore fluid pressure ratio below 25 km, will contribute to a larger stress drop and longer rupture extent in the east fault region.

Another key fault zone parameter governing coseismic fault strength evolution, the characteristic slip distance of the state variable D_{rs} , plays a critical role in the termination of dynamic rupture on the eastern fault, whereas the value of this parameter is not well-constrained for natural faults. For example, Bayesian inversion for seismic source properties using dense regional networks suggests that the critical slip distance D_c of the linear slip weakening friction they assume, which could be associated with D_{rs} to the first order, is one of the least constrained and most heterogeneous frictional parameters (Gallovic et al., 2019).

To match key rupture kinematics, we constrained the first-order distribution of D_{rs} , such as the spontaneous rupture arrest after 140 km of rupture fault, or the amount of shallow slip amplitude. In addition, we test models based on three alternative ways of parameterizing D_{rs} heterogeneity, verifying the influence of the assumed variations of D_{rs} (Section 4.4). The first model assumes along-strike segmentation D_{rs} as shown in Figure S3c. The second model assumes one additional circular patch at shallower depths with reduced D_{rs} (Figure S3b), in addition to the assumption in the preferred model (Figure S3a). The third model assumes D_{rs} scaling with fault coupling coefficient on the fault (Figure S3d). All models result in rupture arrest on the eastern fault and associated surface deformation, confirming the high sensitivity of rupture dynamics and complexities to the assumed fault zone frictional properties.

We find that the distribution of D_{rs} is important in reproducing the surface deformation. For instance, the size and depth of the second patch with reduced D_{rs} in alternative model 2 significantly influence the shallower fault slip amplitudes and the extent and consequently surface displacement at AC13. By trial-and-error, we gradually shift the eastern patch eastward of reduced D_{rs} and increase its radius from 40 to 60 km along the strike direction to better match the inferred moment release and the observed surface displacement at AC13 (Section 4.4; Figure S5). A shallower and more eastward-extended patch increases the amplitude of the second peak in moment release and amplifies displacements recorded at station AC13. This alternative model results in a larger, shallower slip, consequently leading to overestimated displacements at station AC13 (Figure S5).

4.4 Sensitivity of dynamic rupture models

4.4.1 *On-fault heterogeneity of characteristic slip distance D_{rs}*

The on-fault heterogeneity of characteristic slip distance plays a crucial role in the rupture dynamics and kinematics, and consequently, surface displacements at GNSS stations.

We test models with three alternative types of heterogeneity, while the absolute values fall in a limited range (i.e. 0.12 - 0.8 m), for the distribution of characteristic distance in rate-and-state friction law: 1) two circular patches at deeper and shallower depths with reduced $D_{rs} = 0.12$ m while anywhere else has $D_{rs} = 0.8$ m, similar as the setup of the preferred model, 2) along-strike segmentation of two different D_{rs} , and 3) D_{rs} scales with fault coupling coefficient on the fault. We show the distribution of these three types of D_{rs} on faults in Figure S3, respectively.

We find that the choice of on-fault distribution of D_{rs} substantially influences the total extent of the rupture, particularly towards both the eastern and shallower faults. In the models with type 1), the slip continuously propagates to the eastern with an increasing slip rate (Figure S5). In the models of type 2), the slip gradually stops extending to the west while shifting to the shallower depths and finally stops before the eastern edge. The models of type 2) result in a similar distribution of fault slip between 10 and 40 km, while distinguished in the shallower rupture extent compared to our preferred model. The models of 2) produce too large, shallower slips when the size of the second patch is larger, and thus overpredict the surface GPS displacements at site AC13. The results are presented in Fig. ??.

In the alternative models of type 3), the characteristic slip distance parameter D_{rs} scales with fault coupling and thus has a more spatially heterogeneous distribution (Figure S3d). The modeled rupture has a similar slip amplitude in the first 70 km along the strike while growing with a much larger slip amplitude propagating eastward along the fault (Figure S3b). It extends to the edge of the fault and results in a moment magnitude up to 8.4 (Figure S3a). This model with heterogeneous D_{rs} scaling and fault coupling suggests the complex dependence of the rupture process on friction parameters.

4.4.2 Fault zone thermal pressurization heterogeneity

We explore a few combinations of these two parameters and the modeled result shown in Figure S8, considering the possible variations of the theoretical studies (Rempel & Rice, 2006). We chose increased hydraulic diffusivity ($\alpha_{hy} = 10^{-4}$ m/s) and reduced shear zone half-width ($w_f = 0.01$ m) in a larger zone (Zone a), compared with those in the preferred model (Figure S8a). This model can reproduce a run-away rupture with a much longer along-strike extent in the eastern end (Figure S8b). This alternative test demonstrates how thermal pressurization parameters will impact the coseismic rupture on the deep fault.

4.4.3 Impact of 3D shear velocity structure

We use the latest 3D shear velocity model for the eastern Aleutian-Alaska subduction zone from S. Li et al. (2016), which incorporates broadband data from seafloor and land-based seismographs to investigate along-strike variations in structure (Figure S12). We calculated the 3D P-wave velocity model using the averaged V_p/V_s ratio being 1.732. We keep the same 1D density model from Berg et al. (2020). The dynamic rupture simulations with the 3D velocity model are compared the results with our preferred simulation (Figure S13). We need to reduce the overall stress amplitude used in the preferred model by 11 % to have a comparable magnitude (i.e., Mw8.2), given the new 3D shear velocity.

We avoid further parameter-tuning to keep the setup consistent with our preferred model. The rupture dynamics remain the same as our previous model, with minor differences. We found slight differences in fault slip rate and accumulated slip at shallow depths, with negligible impact on the overall rupture dynamics or key findings. The fault slip and moment release plots are shown in Figure S12. The new model has a slight increase in moment release starting at 40 s due to the lower shallow shear velocity (Figure S12). This sensitivity test demonstrates that 3D velocity structure, especially the shallower low shear velocity zone reported in Alaska, is important in modulating the megathrust rupture behavior as observed in most subduction zones (Z. Li et al., 2024c; Ulrich et al., 2019).

4.5 Slip behavior and subduction fault zone heterogeneity

We summarize the slip behaviors of the plate interface in the Aleutian-Alaska subduction zone throughout earthquake cycles in Fig.9. Zhao et al. (2022) propose a model of persistent locked asperities that remain locked over earthquake cycles. These asperities are fully

locked during the interseismic period and are surrounded by partially coupled, conditionally stable (e.g., aseismic slip), or freely creeping regions. Various fault zone processes can significantly influence the balance between the long-term energy buildup and fault weakening mechanisms (Ulrich et al., 2022; Okubo et al., 2019; Plata-Martinez et al., 2021; Elliott et al., 2022; Brooks et al., 2023; He et al., 2023).

Our models, which incorporate faults governed by both rate-and-state friction and thermal pressurization of pore fluid, show that thermally-activated fault weakening, expressed as a substantial increase in pore fluid pressure, can facilitate sustained rupture propagation (Noda & Lapusta, 2013; Vyas et al., 2023). Our choice of hydro-thermal parameters suggests a strong contrast in thermal and hydraulic properties between the eastern and western sections of the Semidi gap. This contrast might explain the different rupture areas or the 2021 and 1938 Semidi events and could impact seismic velocities in active source imaging, as shown by J. Li et al. (2018), as well as rupture dynamics and the seismic hazard. The 1D thermal pressurization model is simplified for a subduction slab by assuming a large, constant permeability gradient along the fault-normal direction. In contrast, pore-fluid evolution with spatially variable permeability along the fault-parallel direction has been investigated in a few theoretical studies. (Ozawa et al., 2024; Zhu et al., 2020)

Our numerical models confirm that the multiple factors related to the fault shear zones, including pore fluid pressure, frictional property, and weakening mechanisms, jointly determine the rupture dynamics in the Chignik event. The trade-offs and thus, ambiguity between different model parameters influencing eventual rupture characteristics is clearly the biggest challenge in exploring these multi-physics numerical models. We note that, with increasing near-source observations, our models offer only one possible mechanical explanation for the conditions that lead to the Chignik earthquake, and other factors, such as stress and strength heterogeneities or fluid-related evolution, may also contribute to its occurrence.

The 2021 Chignik event has struck the deeper portion of Semidi segment with only minor overlap with the 1938 Mw8.3 tsunamigenic earthquake (Freymueller et al., 2021; Ye et al., 2022), confirmed by our dynamic rupture model and the published kinematic inversion (Ye et al., 2022). While the offshore rupture generated less ground shaking in Alaska Peninsula, it still impacted nearby islands (Supporting Information Text S2; Figure S11). We emphasize that using physics-based numerical simulation can help us better understand the

potential seismic and tsunami hazard, especially if the observational network is not densely implemented. This event has raised the question of how regional tectonics may influence long-term seismic and tsunami hazards. The relatively small local tsunami amplitudes triggered by the 2021 Chignik earthquake, along with our tsunami modeling, confirms that deep subduction ruptures have a limited influence on tsunami generation (Supporting Information Text S1). However, estimates of the 1938 M_w 8.3 Semidi event's rupture area vary significantly from the inferences based on aftershock distribution, which remains uncertain due to sparse seismic station coverage (Frey Mueller et al., 2021). The slip deficit since 1938 is estimated up to 5 m, posing a high potential for both seismic and tsunamis hazards in the future. A better understanding the mechanical conditions in this overlap region is crucial for improving tsunami hazard assessments in subduction zones (Olsen et al., 1997; Ulrich et al., 2022; B. Li et al., 2023; W. Meng et al., 2018; D. Liu et al., 2022). Characterizing tsunamigenic and dynamic ruptures using advanced numerical modeling is essential for improving hazard mitigation on a global scale (Kutschera et al., 2024).

5 Conclusions

We demonstrate that the complex structure and physics of the eastern Aleutian-Alaska subduction zone strongly influence megathrust earthquake nucleation and rupture dynamics, rendering them critical considerations for physics-based seismic and tsunami hazard assessment. Specifically, we highlight the role of along-strike variations in fault zone properties in governing rupture propagation and arrest, with implications for regional seismic and tsunami hazards.

By integrating dynamic fault weakening mechanisms and geodetically constrained plate deficit models, we develop a physically viable 3D dynamic rupture scenario that reproduces key kinematic features of the 2021 M_w 8.2 Chignik earthquake. Our array- and frequency-dependent back-projection analyses further demonstrate the consistent rupture characteristics with the preferred model, highlighting the role of shear zone heterogeneities on coseismic earthquake rupture initiation, propagation, and arrest. Our simulations and back-projection analyses further confirm that multiple locked asperities may rupture coseismically, depending on the interplay between stress, strength, and local fault characteristics. Our results demonstrate that thermally activated dynamic weakening, driven by coseismic temperature rise and pore fluid pressurization, facilitates rupture initiation at depths near

the brittle-ductile transition and sustains rupture along the deeper portions of the subduction interface.

Tsunami modeling based on the time-dependent surface displacements from our preferred model is consistent with the relatively small observed tsunami amplitudes triggered by a deeply buried rupture. While the Chignik earthquake primarily ruptured the deep megathrust and generated a modest tsunami, its interaction with the shallow segment of the 1938 M_w 8.3 Semidi event may imply potential for future megathrust ruptures with significant tsunami risk. Our study emphasizes the need for improved observational constraints on fault zone heterogeneity to enhance hazard assessments in the eastern Aleutian-Alaska subduction zone.

Open Research

We use the SeisSol (main branch; commit 040d6c5) available on Github (<https://github.com/SeisSol/SeisSol>). The procedure to download and run the code is described in the SeisSol documentation (seissol.readthedocs.io/en/latest/). We use GeoClaw (v5.9.0) to simulate the sealevel change and tsunami waves in the northern Pacific ocean (<https://github.com/clawpack/geoclaw>).

The authors declare that all data supporting the findings of this study are available within the paper and its Methods section. In particular, all parameter files required for reproducing the dynamic rupture using SeisSol can be downloaded from 10.5281/zenodo.11531700. We provide a detailed README file summarizing the data and data formats provided.

We use code WGS84UTM Mercator 11S for projecting Cartesian coordinates. We download GNSS series data sampled at 1 Hz from EarthScope (formerly Unavco) (<https://www.unavco.org/event-response/july-28-2021-m-8-2-alaska-earthquake/>). The processed static GNSS data arising from co-seismic rupture can be downloaded from EarthScope (<https://www.unavco.org/event-response/july-28-2021-m-8-2-alaska-earthquake/>). The 15-arcsec resolution bathymetry is downloaded from the GEBCO dataset (<https://download.gebco.net/>)

Acknowledgements

We thank Editor Satoshi Ide, the Associate Editor, and the two anonymous reviewers for their constructive comments and suggestions, which have significantly improved the quality of the manuscript. We thank Iyan Mulia for sharing their gauge and DART data. We

thank James Biemiller, Songqiao Shawn Wei, Bin Zhao and Xiaoming Wang for insightful discussions.

Teleseismic body wave waveforms were downloaded from the Incorporated Research Institutions for Seismology (IRIS) data management center (http://ds.iris.edu/wilber3/find_event). Global Centroid Moment Tensor Solutions are from <https://www.globalcmt.org/CMTsearch.html>. Earthquake information is based on the catalogs from National Earthquake Information Center at U.S. Geological Survey (USGS-NEIC) (<https://earthquake.usgs.gov/earthquakes>) and Alaska Earthquake Center (<http://earthquake.alaska.edu>).

The authors acknowledge funding from the National Science Foundation (grant nos. EAR-2225286, EAR-2121568, OAC-2139536, OAC-2311208), from the European Union's Horizon 2020 research and innovation programme (TEAR ERC Starting; grant no. 852992) and Horizon Europe (ChEESE-2P, grant no. 101093038; DT-GEO, grant no. 101058129; and Geo-INQUIRE, grant no. 101058518), National Aeronautics and Space Administration (grant no. 80NSSC20K0495) and King Abdullah University of Science and Technology (KAUST, Grant BAS/1/1339-01-01). D.L. acknowledges LMU Postdoc Support Fund (Excellent Fellowship) and funding from the New Zealand Ministry of Business, Innovation, and Employment to Earth Sciences New Zealand (formerly GNS Science) via the National Seismic Hazard Model 2022 Revision Project (Contract Number 2020-BD101).

Computing resources were provided by the Institute of Geophysics of LMU Munich (Oeser et al., 2006) the Leibniz Supercomputing Center (LRZ projects No. pr63qo and pr45ha on SuperMUC), and the New Zealand Science Infrastructure (NeSI) high-performance computing facilities (No. gns04005).

Author contributions statement

Conceptualization: DL, BL, AAG, RB Methodology: DL, BL, AAG, TU, SY Software: DL, BL, AAG, TU, SY Validation: DL, BL, AAG, TU, SY Resources: DL, BL, AAG, KW, RB Formal Analysis: DL, BL, KW Investigation: DL, BL Data Curation: DL Visualization: DL, BL Funding acquisition: DL, AAG Supervision: AAG Project Administration: AAG Writing - Original Draft: DL, BL Writing - Review and Editing: DL, BL, AAG, TU, SY, KW, RB

Additional information

Competing interests

The authors declare no competing interests.

References

- Aochi, H., & Madariaga, R. (2003). The 1999 Izmit, Turkey, earthquake: Non-planar fault structure, dynamic rupture process, and strong ground motion. *Bulletin of the Seismological Society of America*, 93(3), 1249-1266. doi: 10.1785/0120020167
- Arnulf, A. F., Bassett, D., Harding, A. J., Kodaira, S., Nakanishi, A., & Moore, G. (2022). Upper-plate controls on subduction zone geometry, hydration and earthquake behaviour. *Nature Geosci.*, 15(2), 143-148. doi: 10.1038/s41561-021-00879-x
- Berg, E. M., Lin, F.-C., Allam, A., Schulte-Pelkum, V., Ward, K. M., & Shen, W. (2020). Shear velocity model of Alaska via joint inversion of Rayleigh wave ellipticity, phase velocities, and receiver functions across the Alaska Transportable Array. *J. Geophys. Res.*, 125(2), e2019JB018582. doi: <https://doi.org/10.1029/2019JB018582>
- Boyd, T. M., Taber, J. J., Lerner-Lam, A. L., & Beavan, J. (1988). Seismic rupture and arc segmentation within the Shumagin Islands Seismic Gap, Alaska. *Geophys. Res. Lett.*, 15(3), 201-204. doi: <https://doi.org/10.1029/GL015i003p00201>
- Breuer, A., Heinecke, A., & Bader, M. (2016). Petascale local time stepping for the ADER-DG finite element method. In *2016 IEEE International Parallel and Distributed Processing Symposium (IPDPS)* (p. 854-863). doi: 10.1109/IPDPS.2016.109
- Brooks, B. A., Goldberg, D., DeSanto, J., Ericksen, T. L., Webb, S. C., Nooner, S. L., ... Nevitt, J. (2023). Rapid shallow megathrust afterslip from the 2021 M8.2 Chignik, Alaska earthquake revealed by seafloor geodesy. *Science Advances*, 9(17), eadf9299. doi: [doi:10.1126/sciadv.adf9299](https://doi.org/10.1126/sciadv.adf9299)
- Bruhat, L., & Segall, P. (2016). Coupling on the northern Cascadia subduction zone from geodetic measurements and physics-based models. *J. Geophys. Res.*, 121(11), 8297-8314. doi: 10.1002/2016jb013267
- Cattania, C., & Segall, P. (2021). Precursory slow slip and foreshocks on rough faults.

- 863 *Journal of Geophysical Research: Solid Earth*, 126(4), e2020JB020430. doi:
 864 <https://doi.org/10.1029/2020JB020430>
- 865 Chen, K., Avouac, J.-P., Geng, J., Liang, C., Zhang, Z., Li, Z., & Zhang, S. (2022).
 866 The 2021 Mw 7.4 Madoi earthquake: An archetype bilateral slip-pulse rupture
 867 arrested at a splay fault. *Geophysical Research Letters*, 49(2), e2021GL095243.
- 868 Cocco, M., Aretusini, S., Cornelio, C., Nielsen, S. B., Spagnuolo, E., Tinti, E., &
 869 Di Toro, G. (2023, May). Fracture energy and breakdown work during earth-
 870 quakes. *Annual Review of Earth and Planetary Sciences*, 51(1), annurev-earth-
 871 071822-100304. doi: 10.1146/annurev-earth-071822-100304
- 872 Davies, J., Sykes, L., House, L., & Jacob, K. (1981). Shumagin Seismic Gap, Alaska
 873 Peninsula: History of great earthquakes, tectonic setting, and evidence for high
 874 seismic potential. *J. Geophys. Res.*, 86(B5). doi: 10.1029/JB086iB05p03821
- 875 Day, S. M. (1982). Three-dimensional simulation of spontaneous rupture: the effect of
 876 nonuniform prestress. *Bulletin of the Seismological Society of America*, 72(6A),
 877 1881–1902.
- 878 Day, S. M., Dalgner, L. A., Lapusta, N., & Liu, Y. (2005). Comparison of finite differ-
 879 ence and boundary integral solutions to three-dimensional spontaneous rupture.
 880 *J. Geophys. Res.*, 110(B12). doi: <https://doi.org/10.1029/2005JB003813>
- 881 Dieterich, J. H. (1979). Modeling of rock friction: 1. Experimental results and con-
 882 stitutive equations. *Journal of Geophysical Research: Solid Earth (1978–2012)*,
 883 84(B5), 2161–2168.
- 884 Di Toro, G., Han, R., Hirose, T., De Paola, N., Nielsen, S., Mizoguchi, K., ... Shi-
 885 mamoto, T. (2011). Fault lubrication during earthquakes. *Nature*, 471, 494. doi:
 886 10.1038/nature09838
- 887 Drooff, C., & Freymueller, J. T. (2021). New constraints on slip deficit on the
 888 Aleutian megathrust and inflation at Mt. Veniaminof, Alaska from repeat
 889 GPS measurements. *Geophys. Res. Lett.*, 48(4), e2020GL091787. doi:
 890 <https://doi.org/10.1029/2020GL091787>
- 891 Dumbser, M., & Käser, M. (2006). An arbitrary high-order discontinuous Galerkin
 892 method for elastic waves on unstructured meshes – II. The three-dimensional
 893 isotropic case. *Geophys. J. Int.*, 167(1), 319–336. doi: 10.1111/j.1365-246X.2006
 894 .03120.x
- 895 Dunham, E. M., Belanger, D., Cong, L., & Kozdon, J. E. (2011). Earthquake rup-

- 896 tures with strongly rate-weakening friction and off-fault plasticity, Part 1: Planar
 897 faults. *Bull. Seismol. Soc. Am.*, *101*(5), 2296-2307. doi: 10.1785/0120100075
- 898 Dziewonski, A. M., & Anderson, D. L. (1981). Preliminary reference earth model.
 899 *Physics of the earth and planetary interiors*, *25*(4), 297–356.
- 900 Eberhart-Phillips, D., Christensen, D. H., Brocher, T. M., Hansen, R., Ruppert,
 901 N. A., Haeussler, P. J., & Abers, G. A. (2006). Imaging the transition
 902 from Aleutian subduction to Yakutat collision in central Alaska, with lo-
 903 cal earthquakes and active source data. *J. Geophys. Res.*, *111*(B11). doi:
 904 <https://doi.org/10.1029/2005JB004240>
- 905 Elliott, J. L., Grapenthin, R., Parameswaran Revathy, M., Xiao, Z., Freymueller Jef-
 906 frey, T., & Fusso, L. (2022). Cascading rupture of a megathrust. *Science Ad-
 907 vances*, *8*(18), eabm4131. doi: 10.1126/sciadv.abm4131
- 908 Erickson, B. A., Jiang, J., Lambert, V., Barbot, S. D., Abdelmeguid, M., Almquist,
 909 M., ... Yang, Y. (2023). Incorporating full elastodynamic effects and dipping
 910 fault geometries in community code verification exercises for simulations of earth-
 911 quake sequences and aseismic slip (SEAS). *Bulletin of the Seismological Society
 912 of America*. doi: 10.1785/0120220066
- 913 Freymueller, J. T., Suleimani, E. N., & Nicolisky, D. J. (2021). Constraints on the
 914 slip distribution of the 1938 Mw 8.3 Alaska peninsula earthquake from tsunami
 915 modeling. *Geophys. Res. Lett.*, *48*(9). doi: 10.1029/2021gl092812
- 916 Gallovic, F., Valentová, L., Ampuero, J.-P., & Gabriel, A.-A. (2019). Bayesian dy-
 917 namic finite-fault inversion: 2. Application to the 2016 Mw 6.2 Amatrice, Italy,
 918 earthquake. *J. Geophys. Res.*, *124*(7), 6970-6988. doi: [https://doi.org/10.1029/
 919 2019JB017512](https://doi.org/10.1029/2019JB017512)
- 920 Galvez, P., Ampuero, J.-P., Dalguer, L. A., Somala, S. N., & Nissen-Meyer, T. (2014).
 921 Dynamic earthquake rupture modelled with an unstructured 3-D spectral element
 922 method applied to the 2011 M9 Tohoku earthquake. *Geophys. J. Int.*, *198*(2),
 923 1222-1240. doi: 10.1093/gji/ggu203
- 924 Gao, X., & Wang, K. (2017). Rheological separation of the megathrust seismogenic
 925 zone and episodic tremor and slip. *Nature*, *543*(7645), 416-419. doi: 10.1038/
 926 nature21389
- 927 Geng, J., Chen, X., Pan, Y., Mao, S., Li, C., Zhou, J., & Zhang, K. (2019). PRIDE
 928 PPP-AR: an open-source software for GPS PPP ambiguity resolution. *GPS Solu-*

- tions, 23, 1–10.
- Griffiths, D. V. (1990). Failure criteria interpretation based on Mohr-Coulomb friction. *Journal of Geotechnical Engineering*, 116(6), 986–999. doi: doi:10.1061/(ASCE)0733-9410(1990)116:6(986)
- Guo, H., McGuire, J. J., & Zhang, H. (2021). Correlation of porosity variations and rheological transitions on the southern Cascadia megathrust. *Nature Geoscience*, 14(5), 341–348. doi: 10.1038/s41561-021-00740-1
- Hardebeck, J. L. (2015). Stress orientations in subduction zones and the strength of subduction megathrust faults. *Science*, 349(6253), 1213–1216. doi: https://doi.org/10.1126/science.aac5625s
- Harris, R. A., Barall, M., Aagaard, B. T., Ma, S., & et al. (2018). A suite of exercises for verifying dynamic earthquake rupture codes. *Seismological Research Letters*, 89(3), 1146–1162. (10.1785/0220170222) doi: 10.1785/0220170222
- Harris, R. A., Barall, M., Archuleta, R., Dunham, E., Aagaard, B., Ampuero, J. P., ... Templeton, E. (2009). The SCEC/USGS dynamic earthquake rupture code verification exercise. *Seismol. Res. Lett.*, 80(1), 119–126. doi: 10.1785/gssrl.80.1.119
- Hayes, G. P., Moore, G. L., Portner, D. E., Hearne, M., Flamme, H., Furtney, M., & Smoczyk, G. M. (2018). Slab2, a comprehensive subduction zone geometry model. *Science*.
- He, B., Wei, X., Wei, M., Shen, Y., Alvarez, M., & Schwartz, S. Y. (2023). A shallow slow slip event in 2018 in the Semidi segment of the Alaska subduction zone detected by machine learning [Journal Article]. *Earth and Planetary Science Letters*, 612. doi: 10.1016/j.epsl.2023.118154
- Heinecke, A., Breuer, A., Rettenberger, S., Bader, M., Gabriel, A., Pelties, C., ... Dubey, P. (2014). Petascale high order dynamic rupture earthquake simulations on heterogeneous supercomputers [Conference Proceedings]. In *SC '14: Proceedings of the International Conference for High Performance Computing, Networking, Storage and Analysis* (p. 3–14). doi: 10.1109/SC.2014.6
- Herman, M. W., & Furlong, K. P. (2021). Triggering an unexpected earthquake in an uncoupled subduction zone. *Science Advances*, 7(13), eabf7590. doi: doi:10.1126/sciadv.abf7590
- Hirono, T., Tsuda, K., Tanikawa, W., Ampuero, J. P., Shibasaki, B., Kinoshita, M., & Mori, J. J. (2016). Near-trench slip potential of megaquakes evaluated from fault

- properties and conditions. *Scientific reports*, 6, 28184. doi: 10.1038/srep28184
- Hok, S., Fukuyama, E., & Hashimoto, C. (2011). Dynamic rupture scenarios of anticipated Nankai-Tonankai earthquakes, southwest Japan. *J. Geophys. Res.*, 116(B12). doi: <https://doi.org/10.1029/2011JB008492>
- Ichinose, G., Somerville, P., Thio, H. K., Graves, R., & O’Connell, D. (2007). Rupture process of the 1964 Prince William Sound, Alaska, earthquake from the combined inversion of seismic, tsunami, and geodetic data. *J. Geophys. Res.*, 112(B7). doi: <https://doi.org/10.1029/2006JB004728>
- Ishii, M., Shearer, P. M., Houston, H., & Vidale, J. E. (2005). Extent, duration and speed of the 2004 Sumatra–Andaman earthquake imaged by the Hi-Net array. *Nature*, 435(7044), 933–936.
- Jia, Z., Jin, Z., Marchandon, M., Ulrich, T., Gabriel, A.-A., Fan, W., ... Fialko, Y. (2023). The complex dynamics of the 2023 Kahramanmaras, Turkey, Mw7.8–7.7 earthquake doublet. *Science*, 381(6661), 985–990. doi: [doi:10.1126/science.adi0685](https://doi.org/10.1126/science.adi0685)
- Jiang, J., Erickson, B. A., Lambert, V. R., Ampuero, J., Ando, R., Barbot, S. D., ... van Dinther, Y. (2022). Community-driven code comparisons for three-dimensional dynamic modeling of sequences of earthquakes and aseismic slip. *J. Geophys. Res.*, 127(3). doi: [10.1029/2021jb023519](https://doi.org/10.1029/2021jb023519)
- Kaneko, Y., Avouac, J.-P., & Lapusta, N. (2010). Towards inferring earthquake patterns from geodetic observations of interseismic coupling. *Nature Geosci.*, 3(5), 363–369. doi: [10.1038/NGEO843](https://doi.org/10.1038/NGEO843)
- Kaneko, Y., Fukuyama, E., & Hamling, I. J. (2017). Slip-weakening distance and energy budget inferred from near-fault ground deformation during the 2016 Mw7.8 Kaikōura earthquake. *Geophysical Research Letters*, 44(10), 4765–4773. doi: <https://doi.org/10.1002/2017GL073681>
- Käser, M., & Dumbser, M. (2006). An arbitrary high-order discontinuous Galerkin method for elastic waves on unstructured meshes - I. The two-dimensional isotropic case with external source terms. *Geophysical Journal International*, 166(2), 855–877. doi: [10.1111/j.1365-246X.2006.03051.x](https://doi.org/10.1111/j.1365-246X.2006.03051.x)
- Kirkpatrick, J. D., Edwards, J. H., Verdecchia, A., Kluesner, J. W., Harrington, R. M., & Silver, E. A. (2020). Subduction megathrust heterogeneity characterized from 3D seismic data. *Nature Geoscience*. doi: [10.1038/s41561-020-0562-9](https://doi.org/10.1038/s41561-020-0562-9)

- 995 Kiser, E., & Ishii, M. (2017). Back-projection imaging of earthquakes. *Annual Review*
996 *of Earth and Planetary Sciences*, *45*, 271–299.
- 997 Konca, A. O., Avouac, J.-P., Sladen, A., Meltzner, A. J., Sieh, K., Fang, P., ... Helm-
998 berger, D. V. (2008). Partial rupture of a locked patch of the Sumatra megath-
999 rust during the 2007 earthquake sequence. *Nature*, *456*(7222), 631–635. doi:
1000 10.1038/nature07572
- 1001 Kutschera, F., Jia, Z., Oryan, B., Wong, J. W. C., Fan, W., & Gabriel, A.-A.
1002 (2024). The multi-segment complexity of the 2024 M_W 7.5 noto penin-
1003 sula earthquake governs tsunami generation [Journal Article]. *Geophysi-*
1004 *cal Research Letters*, *51*(21), e2024GL109790. Retrieved from [https://](https://agupubs.onlinelibrary.wiley.com/doi/abs/10.1029/2024GL109790)
1005 agupubs.onlinelibrary.wiley.com/doi/abs/10.1029/2024GL109790 doi:
1006 <https://doi.org/10.1029/2024GL109790>
- 1007 Lay, T., Kanamori, H., Ammon, C. J., Koper, K. D., Hutko, A. R., Ye, L., ... Rushing,
1008 T. M. (2012). Depth-varying rupture properties of subduction zone megathrust
1009 faults. *J. Geophys. Res.*, *117*(B04311), B04311. doi: [https://doi.org/10.1029/](https://doi.org/10.1029/2011JB009133)
1010 [2011JB009133](https://doi.org/10.1029/2011JB009133)
- 1011 Li, B., Gabriel, A.-A., Ulrich, T., Abril, C., & Halldorsson, B. (2023). Dynamic rup-
1012 ture models, fault interaction and ground motion simulations for the segmented
1013 Húsavík-Flatey Fault Zone, Northern Iceland. *Journal of Geophysical Research:*
1014 *Solid Earth*, *128*(6), e2022JB025886.
- 1015 Li, B., & Ghosh, A. (2017). Imaging rupture process of the 2015 Mw 8.3 Illapel
1016 earthquake using the US Seismic Array. *The Chile-2015 (Illapel) earthquake and*
1017 *tsunami*, 33–43.
- 1018 Li, B., Wu, B., Bao, H., Oglesby, D. D., Ghosh, A., Gabriel, A.-A., ... Chu, R. (2022).
1019 Rupture heterogeneity and directivity effects in back-projection analysis. *Journal*
1020 *of Geophysical Research: Solid Earth*, *127*(3), e2021JB022663.
- 1021 Li, D., & Liu, Y. (2016). Spatiotemporal evolution of slow slip events in a nonpla-
1022 nar fault model for northern Cascadia subduction zone. *J. Geophys. Res.*, *121*(9),
1023 6828–6845. doi: 10.1002/2016jb012857
- 1024 Li, J., Shillington, D. J., Saffer, D. M., Bécel, A., Nedimović, M. R., Kuehn, H., ...
1025 Abers, G. A. (2018). Connections between subducted sediment, pore-fluid
1026 pressure, and earthquake behavior along the Alaska megathrust. *Geology*, *46*,
1027 299–302.

- Li, S., Freymueller, J., & McCaffrey, R. (2016). Slow slip events and time-dependent variations in locking beneath Lower Cook Inlet of the Alaska-Aleutian subduction zone. *J. Geophys. Res.*, *121*(2), 1060-1079. doi: 10.1002/2015jb012491
- Li, Z., Wiens, D. A., Shen, W., & Shillington, D. J. (2024a). Along-strike variations of Alaska subduction zone structure and hydration determined from amphibious seismic data. *J. Geophys. Res.*, *129*(3), e2023JB027800. doi: <https://doi.org/10.1029/2023JB027800>
- Li, Z., Wiens, D. A., Shen, W., & Shillington, D. J. (2024b). Along-strike variations of Alaska subduction zone structure and hydration determined from amphibious seismic data. *Journal of Geophysical Research: Solid Earth*, *129*(3), e2023JB027800. doi: <https://doi.org/10.1029/2023JB027800>
- Li, Z., Wiens, D. A., Shen, W., & Shillington, D. J. (2024c). Along-strike variations of alaska subduction zone structure and hydration determined from amphibious seismic data [Journal Article]. *Journal of Geophysical Research: Solid Earth*, *129*(3), e2023JB027800. doi: <https://doi.org/10.1029/2023JB027800>
- Liu, C., Lay, T., & Xiong, X. (2022). The 29 July 2021 MW 8.2 Chignik, Alaska peninsula earthquake rupture inferred from seismic and geodetic observations: Re-rupture of the western 2/3 of the 1938 rupture zone. *Geophys. Res. Lett.*, *49*(4), e2021GL096004. doi: <https://doi.org/10.1029/2021GL096004>
- Liu, D., Duan, B., Scharer, K., & Yule, D. (2022). Observation-Constrained multicyle dynamic models of the Southern San Andreas and the Northern San Jacinto Faults: Addressing complexity in paleoearthquake extent and recurrence with realistic 2D fault geometry. *Journal of Geophysical Research: Solid Earth*, *127*(2), e2021JB023420.
- López, A. M., & Okal, E. A. (2006). A seismological reassessment of the source of the 1946 Aleutian ‘tsunami’ earthquake. *Geophys. J. Int.*, *165*(3), 835-849. doi: 10.1111/j.1365-246X.2006.02899.x
- Loveless, J. P., & Meade, B. J. (2011). Spatial correlation of interseismic coupling and coseismic rupture extent of the 2011 Mw= 9.0 Tohoku-oki earthquake. *Geophys. Res. Lett.*, *38*(17), n/a-n/a. doi: 10.1029/2011gl048561
- Madden, E. H., Ulrich, T., & Gabriel, A.-A. (2022). The state of pore fluid pressure and 3-D megathrust earthquake dynamics. *J. Geophys. Res.*, *127*(4), e2021JB023382. doi: <https://doi.org/10.1029/2021JB023382>

- 1061 Mai, P. M., Aspiotis, T., Aquib, T. A., Cano, E. V., Castro-Cruz, D., Espindola-
 1062 Carmona, A., ... others (2023). The destructive earthquake doublet of 6 Febru-
 1063 ary 2023 in south-central Türkiye and northwestern Syria: Initial observations
 1064 and analyses. *The Seismic Record*, 3(2), 105–115.
- 1065 Meng, Q., & Duan, B. (2022). Dynamic modeling of interactions between shallow
 1066 slow-slip events and subduction earthquakes. *Seismol. Res. Lett.*. doi: 10.1785/
 1067 0220220138
- 1068 Meng, W., Yoshihiro, K., Pengcheng, S., & Yajing, L. (2018). Numerical model-
 1069 ing of dynamically triggered shallow slow slip events in New Zealand by the
 1070 2016 Mw 7.8 Kaikoura earthquake. *Geophysical Research Letters*, 45(10). doi:
 1071 doi:10.1029/2018GL077879
- 1072 Moreno, M., Li, S., Melnick, D., Bedford, J. R., Baez, J. C., Motagh, M., ... Oncken,
 1073 O. (2018). Chilean megathrust earthquake recurrence linked to frictional contrast
 1074 at depth. *Nature Geosci.*, 11(4), 285–290. doi: 10.1038/s41561-018-0089-5
- 1075 Mulia, I. E., Gusman, A. R., Heidarzadeh, M., & Satake, K. (2022). Sensitivity of
 1076 tsunami data to the up-dip extent of the July 2021 Mw 8.2 Alaska earthquake.
 1077 *Seismol. Res. Lett.*, 93(4), 1992–2003. doi: 10.1785/0220210359
- 1078 Noda, H., Dunham, E. M., & Rice, J. R. (2009). Earthquake ruptures with thermal
 1079 weakening and the operation of major faults at low overall stress levels [Journal
 1080 Article]. *Journal of Geophysical Research*, 114(B7). doi: 10.1029/2008jb006143
- 1081 Noda, H., & Lapusta, N. (2010). Three-dimensional earthquake sequence simula-
 1082 tions with evolving temperature and pore pressure due to shear heating: Ef-
 1083 fect of heterogeneous hydraulic diffusivity. *J. Geophys. Res.*, 115(B12). doi:
 1084 10.1029/2010jb007780
- 1085 Noda, H., & Lapusta, N. (2013). Stable creeping fault segments can become destruc-
 1086 tive as a result of dynamic weakening. *Nature*, 493(7433), 518–521. doi: 10.1038/
 1087 nature11703
- 1088 Oeser, J., Bunge, H.-P., & Mohr, M. (2006). Cluster design in the earth sciences tethys.
 1089 In *International conference on high performance computing and communications*
 1090 (pp. 31–40).
- 1091 Okubo, K., Bhat, H. S., Rougier, E., Marty, S., Schubnel, A., Lei, Z., ... Klinger, Y.
 1092 (2019). Dynamics, radiation, and overall energy budget of earthquake rupture
 1093 with coseismic off-fault damage. *Journal of Geophysical Research: Solid Earth*,

- 1094 124(11), 11771-11801. doi: <https://doi.org/10.1029/2019JB017304>
- 1095 Olsen, K. B., Madariaga, R., & Archuleta, R. J. (1997). Three-dimensional dynamic
1096 simulation of the 1992 Landers earthquake. *Science*, 278(5339), 834-838.
- 1097 Ozawa, S., Ida, A., Hoshino, T., & Ando, R. (2022). Large-scale earthquake sequence
1098 simulations on 3-D non-planar faults using the boundary element method acceler-
1099 ated by lattice H-matrices. *Geophysical Journal International*, 232(3), 1471-1481.
1100 doi: 10.1093/gji/ggac386
- 1101 Ozawa, S., Yang, Y., & Dunham, E. M. (2024). Fault-valve instability: A mech-
1102 anism for slow slip events [Journal Article]. *Journal of Geophysical Re-*
1103 *search: Solid Earth*, 129(10), e2024JB029165. Retrieved from [https://](https://agupubs.onlinelibrary.wiley.com/doi/abs/10.1029/2024JB029165)
1104 agupubs.onlinelibrary.wiley.com/doi/abs/10.1029/2024JB029165 doi:
1105 <https://doi.org/10.1029/2024JB029165>
- 1106 Palgunadi, K. H., Gabriel, A., Ulrich, T., Lopez-Comino, J. A., & Mai, P. M. (2020).
1107 Dynamic Fault Interaction during a Fluid-Injection-Induced Earthquake: The
1108 2017 Mw 5.5 Pohang Event. *Bulletin of the Seismological Society of America*,
1109 110(5), 2328-2349. Retrieved from <https://doi.org/10.1785/0120200106> doi:
1110 10.1785/0120200106
- 1111 Pelties, C., Gabriel, A. A., & Ampuero, J. P. (2014). Verification of an ADER-DG
1112 method for complex dynamic rupture problems. *Geosci. Model Dev.*, 7(3), 847-
1113 866. doi: 10.5194/gmd-7-847-2014
- 1114 Perez-Silva, A., Li, D., Gabriel, A.-A., & Kaneko, Y. (2021). 3D Modeling of long-term
1115 slow slip events along the flat-slab segment in the Guerrero Seismic Gap, Mexico.
1116 *Geophys. Res. Lett.*, 48(13). doi: <https://doi.org/10.1029/2021GL092968>
- 1117 Plata-Martinez, R., Ide, S., Shinohara, M., Garcia, E. S., Mizuno, N., Dominguez,
1118 L. A., ... Ito, Y. (2021). Shallow slow earthquakes to decipher future catas-
1119 trophic earthquakes in the Guerrero seismic gap. *Nature Communications*, 12(1),
1120 3976. doi: 10.1038/s41467-021-24210-9
- 1121 Rempel, A. W., & Rice, J. R. (2006). Thermal pressurization and onset of melt-
1122 ing in fault zones. *J. Geophys. Res.*, 111(B9). doi: [https://doi.org/10.1029/](https://doi.org/10.1029/2006JB004314)
1123 [2006JB004314](https://doi.org/10.1029/2006JB004314)
- 1124 Rice, J. R. (2006). Heating and weakening of faults during earthquake slip. *J. Geophys.*
1125 *Res.*, 111(B5). doi: <https://doi.org/10.1029/2005JB004006>
- 1126 Romanet, P., & Ozawa, S. (2021). Fully dynamic earthquake cycle simulations

- on a nonplanar fault using the spectral boundary integral element method
(sBIEM). *Bulletin of the Seismological Society of America*, 112(1), 78-97. doi:
10.1785/0120210178
- Ruina, A. (1983). Slip instability and state variable friction laws. *J. Geophys. Res.*,
88(B12), 10359. doi: 10.1029/JB088iB12p10359
- Scholz, H. C. (1998). Earthquakes and friction laws. *Nature*, 391. doi: 10.1038/34097
- Simons, M., Minson, S. E., Sladen, A., Ortega, F., Jiang, J., Owen, S. E., ... Webb,
F. H. (2011). The 2011 magnitude 9.0 Tohoku-Oki earthquake: Mosaicking the
megathrust from seconds to centuries. *Science*, 332, 1421-1425.
- Suhendi, C., Li, B., Vasyura-Bathke, H., Liu, J., Jónsson, S., & Mai, P. M. (2025).
Bayesian inversion and quantitative comparison for bilaterally quasi-symmetric
rupture processes on a multisegment fault in the 2021 Mw 7.4 Maduo earthquake.
Geophysical Journal International, 240(1), 673–695.
- Tape, C., Holtkamp, S., Silwal, V., Hawthorne, J., Kaneko, Y., Ampuero, J. P., ...
West, M. E. (2018). Earthquake nucleation and fault slip complexity in
the lower crust of central Alaska. *Nature Geoscience*, 11(7), 536-541. doi:
10.1038/s41561-018-0144-2
- Taufiqurrahman, T., Gabriel, A.-A., Li, D., Ulrich, T., Li, B., Carena, S., ... Gallovič,
F. (2023). Dynamics, interactions and delays of the 2019 Ridgecrest rupture
sequence. *Nature*, 618(7964), 308–315.
- Tinti, E., Spudich, P., & Cocco, M. (2005). Earthquake fracture energy inferred from
kinematic rupture models on extended faults. *J. Geophys. Res.*, 110(B12). doi:
10.1029/2005jb003644
- Ujiie, K., Kameyama, M., & Yamaguchi, A. (2010, April). Geological record of thermal
pressurization and earthquake instability of subduction thrusts. *Tectonophysics*,
485(1-4), 260–268. doi: 10.1016/j.tecto.2010.01.002
- Ulrich, T., Gabriel, A.-A., Ampuero, J.-P., & Xu, W. (2019). Dynamic viability of the
2016 Mw 7.8 Kaikōura earthquake cascade on weak crustal faults. *Nature commu-
nications*, 10(1), 1213. doi: 10.1038/s41467-019-09125-w
- Ulrich, T., Gabriel, A.-A., & Madden, E. H. (2022). Stress, rigidity and sediment
strength control megathrust earthquake and tsunami dynamics. *Nature Geosci.*,
15(1), 67-73. doi: 10.1038/s41561-021-00863-5
- Uphoff, C., Rettenberger, S., Bader, M., Madden, E. H., Ulrich, T., Wollherr, S., &

- 1160 Gabriel, A.-A. (2017). *Extreme scale multi-physics simulations of the tsunami-*
 1161 *genic 2004 sumatra megathrust earthquake*. ACM. doi: 10.1145/3126908.3126948
- 1162 USGS. (Last accessed: 14.10.2024a). [https://earthquake.usgs.gov/earthquakes/](https://earthquake.usgs.gov/earthquakes/eventpage/ak0219neiszm/finite-fault)
 1163 [eventpage/ak0219neiszm/finite-fault](https://earthquake.usgs.gov/earthquakes/eventpage/ak0219neiszm/finite-fault).
- 1164 USGS. (Last accessed: 14.10.2024b). [https://earthquake.usgs.gov/earthquakes/](https://earthquake.usgs.gov/earthquakes/eventpage/ak0219neiszm/origin/detail)
 1165 [eventpage/ak0219neiszm/origin/detail](https://earthquake.usgs.gov/earthquakes/eventpage/ak0219neiszm/origin/detail). (Accessed: 14.10.2024)
- 1166 Viesca, R. C., & Garagash, D. I. (2015). Ubiquitous weakening of faults due to ther-
 1167 mal pressurization. *Nature Geosci.*, 8(11), 875-879. doi: 10.1038/ngeo2554
- 1168 Vigny, C., Socquet, A., Peyrat, S., Ruegg, J.-C., Métois, M., Madariaga, R., ...
 1169 Kendrick, E. (2011). The 2010 Mw8.8 Maule megathrust earthquake of Cen-
 1170 tral Chile, monitored by GPS. *Science*, 332, 1417-1421.
- 1171 von Huene, R., Miller, J. J., & Weinrebe, W. (2012). Subducting plate geology in three
 1172 great earthquake ruptures of the western Alaska margin, Kodiak to Unimak. *Geo-*
 1173 *sphere*, 8(3), 628-644. doi: 10.1130/ges00715.1
- 1174 Vosteen, H.-D., & Schellschmidt, R. (2003). Influence of temperature on thermal
 1175 conductivity, thermal capacity and thermal diffusivity for different types of
 1176 rock. *Physics and Chemistry of the Earth, Parts A/B/C*, 28(9), 499-509. doi:
 1177 [https://doi.org/10.1016/S1474-7065\(03\)00069-X](https://doi.org/10.1016/S1474-7065(03)00069-X)
- 1178 Vyas, J. C., Gabriel, A.-A., Ulrich, T., Mai, P. M., & Ampuero, J.-P. (2023). How does
 1179 thermal pressurization of pore fluids affect 3D strike-slip earthquake dynamics
 1180 and ground motions? *Bulletin of the Seismological Society of America*, 113(5),
 1181 1992-2008.
- 1182 Wang, F., Wei, S. S., Drooff, C., Elliott, J. L., Freymueller, J. T., Ruppert, N. A., &
 1183 Zhang, H. (2024). Fluids control along-strike variations in the Alaska megath-
 1184 rust slip. *Earth Planet. Sci. Lett.*, 633, 118655. doi: [https://doi.org/10.1016/](https://doi.org/10.1016/j.epsl.2024.118655)
 1185 [j.epsl.2024.118655](https://doi.org/10.1016/j.epsl.2024.118655)
- 1186 Weng, H., & Yang, H. (2018). Constraining frictional properties on fault by dynamic
 1187 rupture simulations and near-field observations. *Journal of Geophysical Research:*
 1188 *Solid Earth*, 123(8), 6658-6670. doi: <https://doi.org/10.1029/2017JB015414>
- 1189 Wibberley, C. A. J. (2002). Hydraulic diffusivity of fault gouge zones and implications
 1190 for thermal pressurization during seismic slip. *Earth, Planets and Space*, 54(11),
 1191 1153-1171. doi: 10.1186/BF03353317
- 1192 Wollherr, S., Gabriel, A.-A., & Mai, P. M. (2019). Landers 1992 “reloaded”: Integrative

- dynamic earthquake rupture modeling. *J. Geophys. Res.*, *124*(7), 6666–6702. doi: <https://doi.org/10.1029/2018JB016355>
- Xiao, Z., Freymueller, J. T., Grapenthin, R., Elliott, J. L., Drooff, C., & Fusso, L. (2021). The deep Shumagin gap filled: Kinematic rupture model and slip budget analysis of the 2020 Mw 7.8 Simeonof earthquake constrained by GNSS, global seismic waveforms, and floating InSAR. *Earth Planet. Sci. Lett.*, *576*. doi: 10.1016/j.epsl.2021.117241
- Xu, L., Mohanna, S., Meng, L., Ji, C., Ampuero, J.-P., Yunjun, Z., ... Liang, C. (2023). The overall-subshear and multi-segment rupture of the 2023 Mw7.8 Kahramanmaras, Turkey earthquake in millennia supercycle. *Communications Earth & Environment*, *4*(1), 379. doi: 10.1038/s43247-023-01030-x
- Yang, H., Yao, S., He, B., Newman, A. V., & Weng, H. (2019). Deriving rupture scenarios from interseismic locking distributions along the subduction megathrust. *J. Geophys. Res.*, *124*(10), 10376–10392. doi: 10.1029/2019jb017541
- Ye, L., Bai, Y., Si, D., Lay, T., Cheung, K. F., & Kanamori, H. (2022). Rupture model for the 29 July 2021 Mw 8.2 Chignik, Alaska earthquake constrained by seismic, geodetic, and tsunami observations. *J. Geophys. Res.*, *127*(7), e2021JB023676. doi: <https://doi.org/10.1029/2021JB023676>
- Ye, L., Lay, T., Kanamori, H., Yamazaki, Y., & Cheung, K. F. (2021). The 22 July 2020 Mw 7.8 Shumagin seismic gap earthquake: Partial rupture of a weakly coupled megathrust. *Earth Planet. Sci. Lett.*, *562*, 116879. doi: <https://doi.org/10.1016/j.epsl.2021.116879>
- Yue, H., Lay, T., Schwartz, S. Y., Rivera, L., Protti, M., Dixon, T. H., ... Newman, A. V. (2013). The 5 September 2012 Nicoya, Costa Rica Mw 7.6 earthquake rupture process from joint inversion of high-rate GPS, strong-motion, and teleseismic P wave data and its relationship to adjacent plate boundary interface properties. *Journal of Geophysical Research: Solid Earth*, *118*(10), 5453–5466.
- Zhao, B., Bürgmann, R., Wang, D., Zhang, J., Yu, J., & Li, Q. (2022). Aseismic slip and recent ruptures of persistent asperities along the Alaska-Aleutian subduction zone. *Nature communications*, *13*(1), 3098. doi: 10.1038/s41467-022-30883-7
- Zhu, W., Allison, K. L., Dunham, E. M., & Yang, Y. (2020). Fault valving and pore pressure evolution in simulations of earthquake sequences and aseismic slip [Journal Article]. *Nature Communications*, *11*(1), 4833. Retrieved from

1226 <https://doi.org/10.1038/s41467-020-18598-z><https://www.nature.com/>
1227 [articles/s41467-020-18598-z.pdf](https://www.nature.com/articles/s41467-020-18598-z.pdf) doi: 10.1038/s41467-020-18598-z

parameter	symbol	value	variability
state-evolution parameter	b	0.014	homogeneous
direct-effect parameter	a	0.01 - 0.02	depth-dependent.
critical slip distance	D_{rs}	0.12-0.8 m	heterogeneous
fast-weakening velocity	V_w	0.1 m/s	homogeneous
fast-weakening friction	f_w	0.1	homogeneous
reference velocity	V_0	10^{-6} m/s	homogeneous
reference friction coeff.	f_0	0.6	homogeneous
initial velocity	v_{ini}	10^{-16} m/s	homogeneous
thermal diffusivity	α_{th}	10^{-6} m^2/s	homogeneous
specific heat capacity	ρc	2.7×10^{-6} $MJ/m^3/K$	homogeneous
undrained $\Delta p/\Delta T$	Λ_{th}	0.1 MPa/K	homogeneous
hydraulic diffusivity	α_{hy}	$10^{-8} - 10^{-4}$ m^2/s	heterogeneous.
half-width of shear zone	w	0.035-0.10 m	heterogeneous.

Table 1. Assumed physical parameters in the rate-and-state friction (RSF) used, accounting for the possibility of strong weakening at high slip rates and for the effects of thermal pressurization of pore fluids.

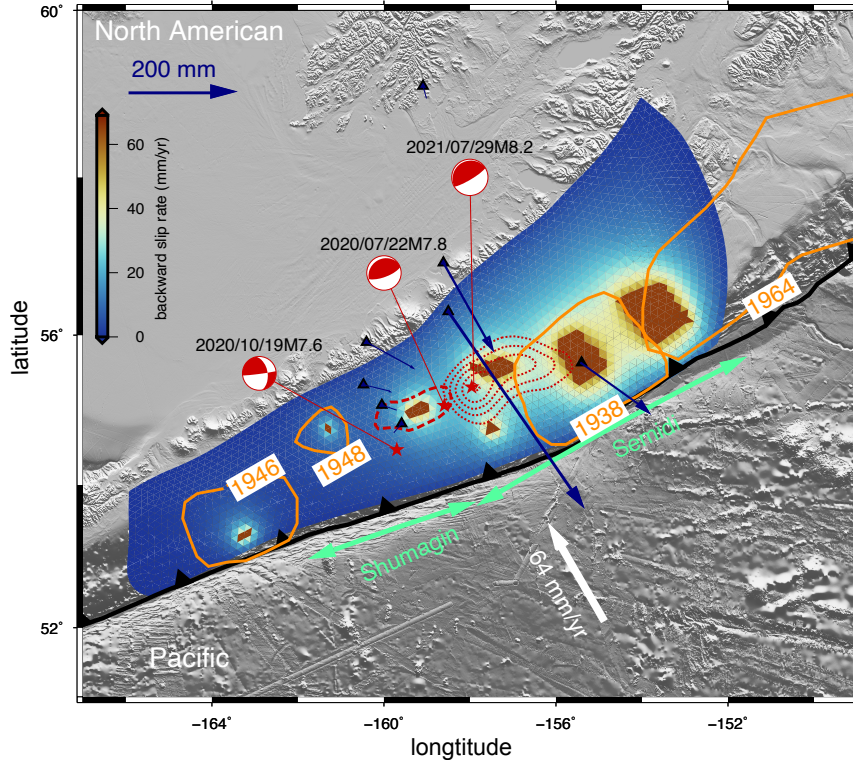


Figure 1. Overview of the 2021 M_w 8.2 Chignik, Alaska earthquake, plate interface coupling, and major historic earthquakes. The interseismic back slip distribution on the fault is from Zhao et al.(2022). The red beachballs indicate the source mechanisms for the major events in 2020 and 2021. The red solid lines indicate the 1-5 m slip contours inferred for the Chignik earthquake from a joint inversion of teleseismic, GNSS, and satellite data (Elliott et al., 2022). The red dashed line delineates the rupture area of the 2020 M7.8 Shumagin earthquake (Elliott et al., 2022). The pale green arrows indicate the Semidi and Shumargin segments along the trench, as inferred from interseismic coupling variations using regional GNSS data (Drooff & Freymueller, 2021). The orange lines indicate the rupture area of several historical earthquakes, including the 1964 M9.2 Prince William Sound, Alaska earthquake (Ichinose et al., 2007), the inferred rupture of the 1938 M8.3 Semidi earthquake (best-fitting model of Freymuller et al. (2021)), the 1946 M8.6 Unimak tsunami earthquake Lopez et al. (López & Okal, 2006), and the 1948 Ms 7.5 earthquake Boyd et al. (Boyd et al., 1988). Seven GNSS stations and the inferred coseismic horizontal displacements of the 2021 M8.2 Chignik are indicated by blue triangles and vectors, for stations with displacement amplitude larger than 0.1 m, respectively.

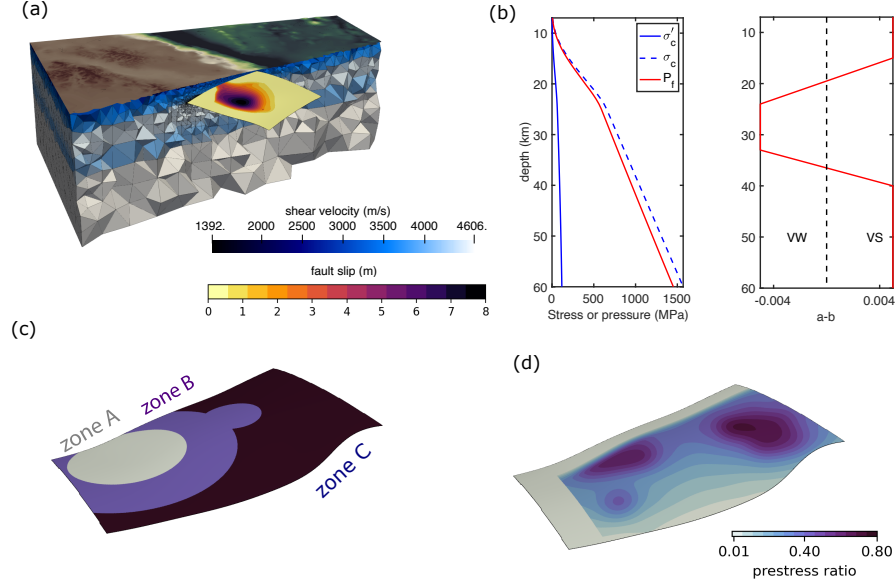


Figure 2. (a) 3D view of topo-bathymetric map (sampled from 10-arc minute of GEBCO dataset), 1D shear velocity (dark-blue-white) from Berg et al. (2020), model tetrahedral mesh and final fault slip of the preferred scenario of the 2021 M8.2 Alaska earthquake. The shallow edge of the fault is located along the -10 km depth contour and extends horizontally from (159.8°W, 54.2°N) to (155.5°W, 55.5°N). The fault surface is meshed into 400 m-long triangles with spatial coarsening away from it (Section 2.1). (b) Profiles of pore fluid pressure ratio, function Omega, effective confining stress and rate-and-state friction stability coefficient ($a-b$) in the preferred model. (c) Spatial distribution of key frictional and thermal pressurization parameters in three zones. Zone A: smaller critical slip distance, smaller half-shear-zone width and higher thermal diffusivity. Zone B: smaller critical slip distance, larger half-shear-zone width and lower thermal diffusivity. Zone C: larger critical slip distance, larger half-shear-zone width and lower thermal diffusivity. More details in Section 3.3. (d) Assumed initial relative prestress ratio R , defined as the potential stress drop over the full breakdown strength drop, constrained by fault geometry and geodetic coupling model (Zhao et al., 2022) (see Section 2.2).

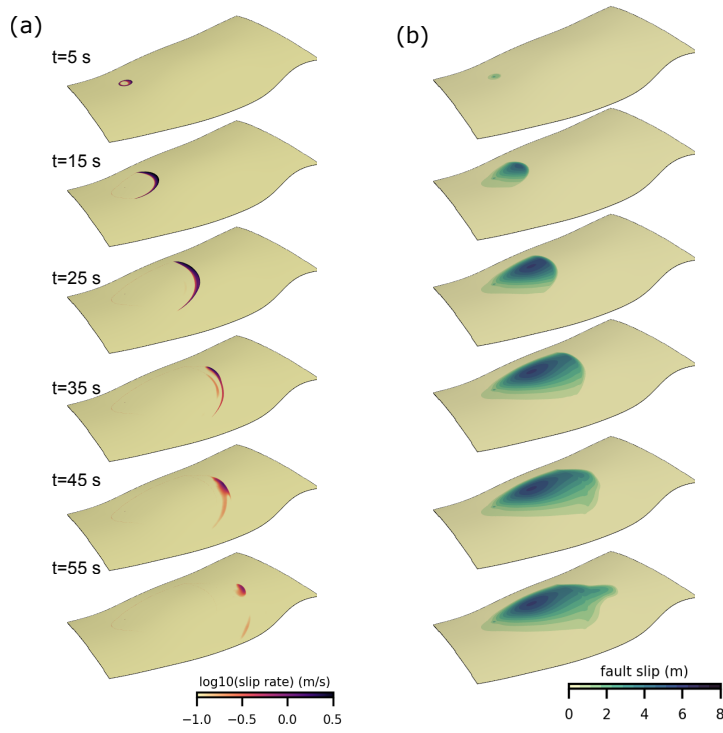


Figure 3. Snapshots of (a) Fault slip rate (in log) and (b) fault slip at various time steps in the preferred model.

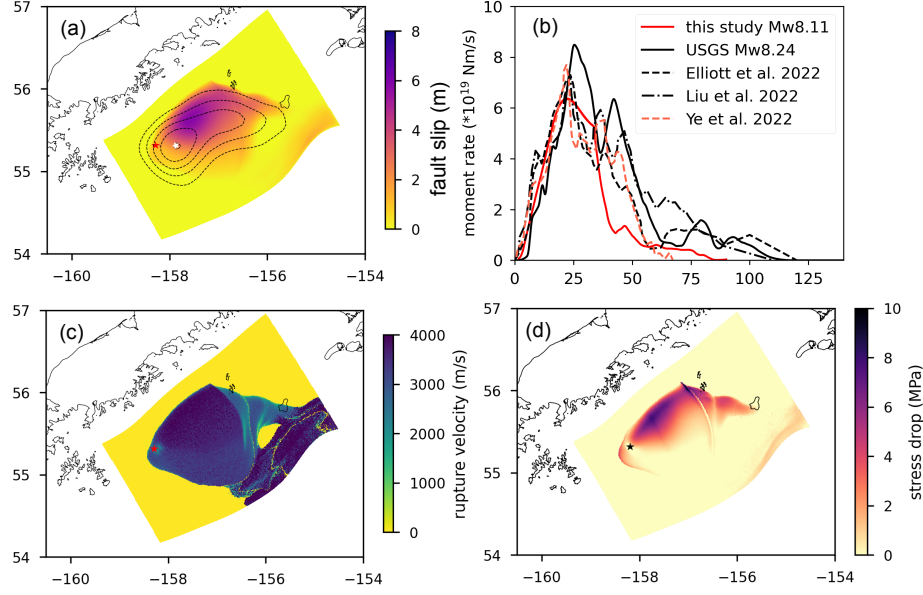


Figure 4. Preferred scenario of the Chignik earthquake. (a) Fault slip, overlain by the 1 m sampled slip contours of Elliott et al. (2022) model. The white and orange stars indicate the epicentral location inferred by USGS (USGS, Last accessed: 14.10.2024b) and the location of nucleation of our preferred model (see Methods "Nucleation"). (b) Moment release rate in the preferred model (solid red), compared with inferences from USGS (USGS, Last accessed: 14.10.2024a) (solid black), and Elliott et al. (2022), Liu et al. (2022), and Ye et al. (2022), respectively. (c) Modelled rupture velocity and (d) Modeled static stress drop.

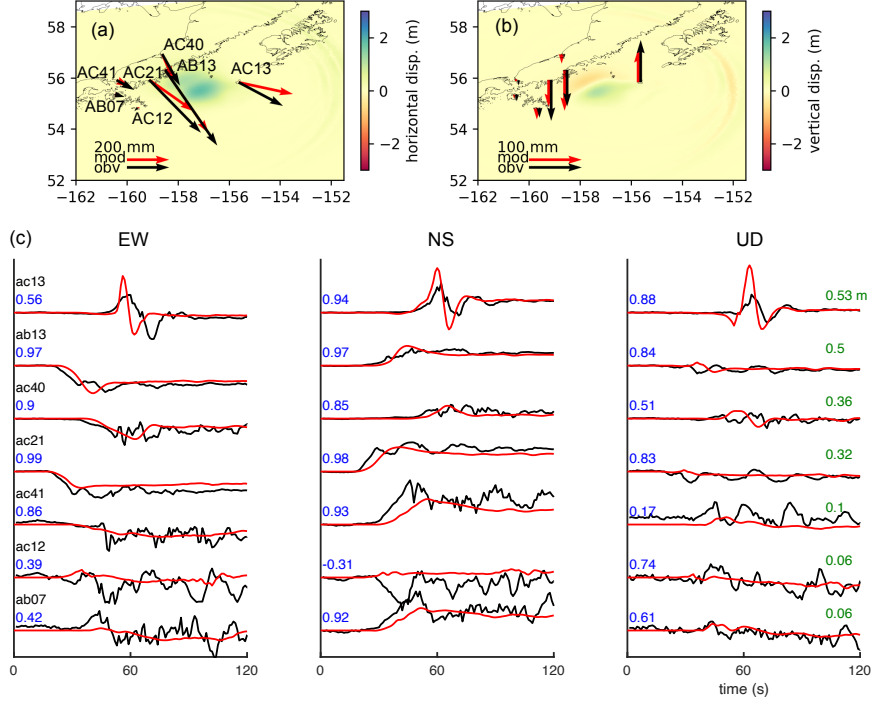


Figure 5. (a) horizontal and (b) vertical components of synthetic and observed static displacement vectors at GNSS stations. Stations are labeled in black. (c) Unfiltered synthetic displacement waveforms (red) at selected high-rate GNSS stations compared with 1 s sampled observations (black). Component-wise cross-correlation coefficients are labeled in blue. The three time series components are scaled by the observed maximum EW amplitude (in meter) at each site, which is labelled in the third column. The stations are ordered by the amplitude.

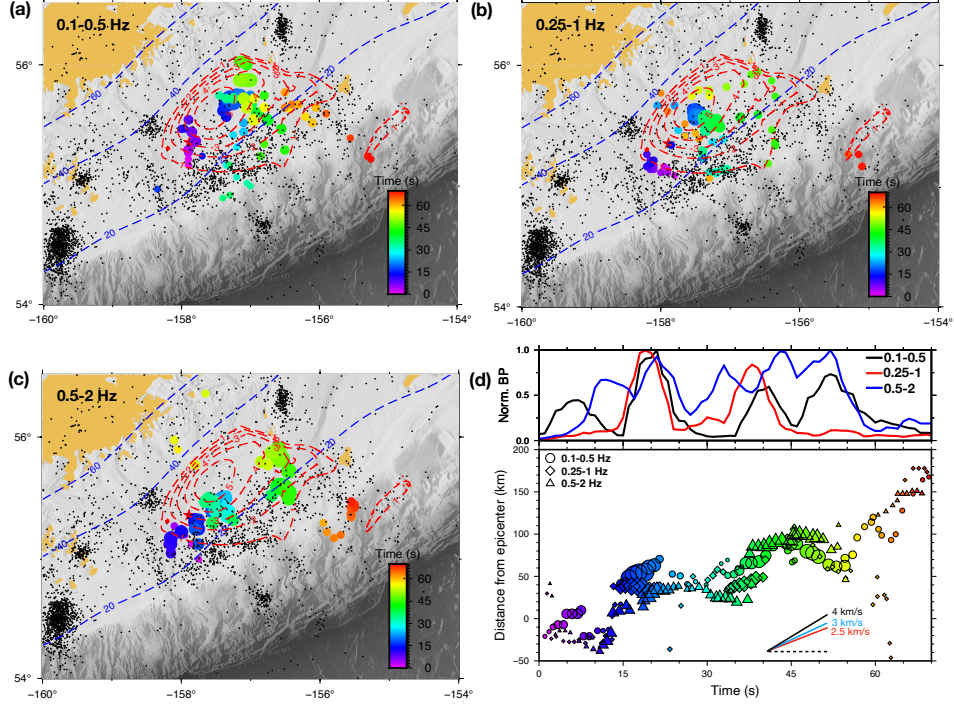


Figure 6. Frequency-dependent back-projection results using the Europe (EU) Array. (a)-(c) show the back-projection imaged rupture process in the frequency range 0.1-0.5, 0.25-1 and 0.5-2 Hz, respectively. The symbol sizes are proportional to the back-projection beam power. Blue dashed lines mark the slab2 model depth contours (Hayes et al., 2018). Red dashed lines show the slip contours of the preferred model. The pink star indicates the nucleation of the preferred model. The black dots show the aftershocks of the Chignik earthquake from the United States Geological Survey (USGS). (d) The relative beam power evolution (top) and rupture propagation distance with time (bottom). Stations of EU array considered are plotted in Fig. ??.

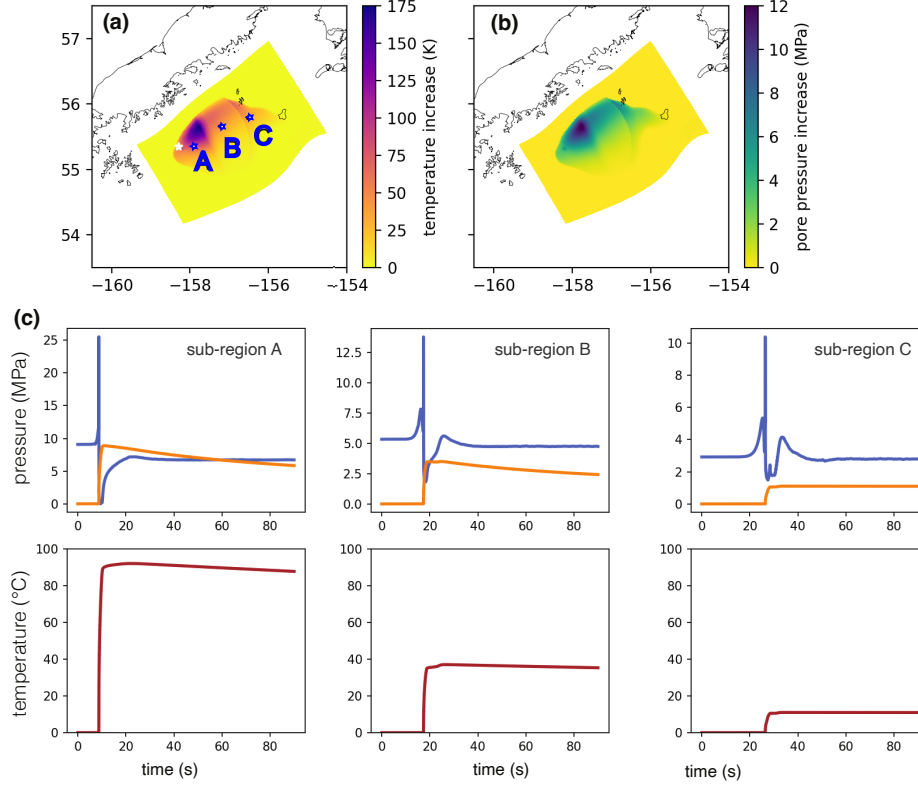


Figure 7. Thermal pressurization weakening. Modeled coseismic on-fault temperature (a) and pore fluid pressure (b) increase, at 140 s simulation time. The blue stars indicate the locations of the three on-fault receivers considered in (c). The nucleation is indicated by the white star. (c) Evolution of shear traction (blue), pore fluid pressure (orange) and temperature (red) with time (s) at selected on-fault receivers. Each receiver samples a sub-region dominated by a different weakening mechanism: 1) stronger TP weakening, rate-and-state friction (RSF) governed by a smaller characteristic slip distance of state evolution D_{rs} , 2) weaker TP weakening and RSF governed by a smaller D_{rs} , and 3) weak TP weakening and RSF governed by a larger D_{rs} , respectively. Note that a slight reduction in T and P as diffusion continues with time.

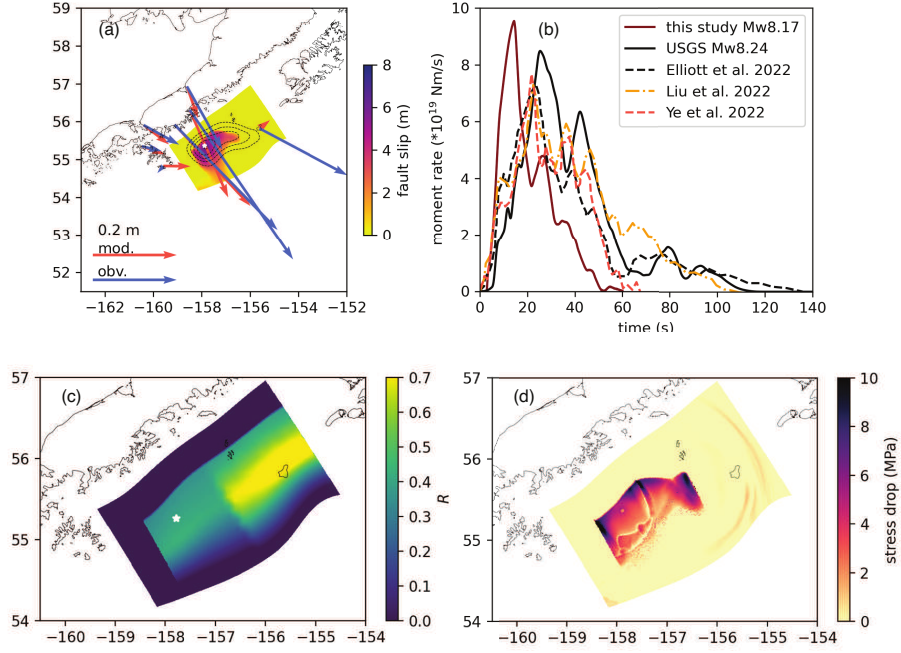


Figure 8. Alternative scenario of the Chignik earthquake constrained by the fault coupling model of Drooff and Freymueller (2021). (a) Fault slip, overlain by the 1 m sampled slip contours of Elliott et al. (2022) model. Synthetic and observed coseismic displacements at GNSS stations are plotted with vectors. (b) Moment release rate in the preferred model (solid red), compared with inferences from USGS (USGS, Last accessed: 14.10.2024a) (solid black), and Elliott et al. (2022), Liu et al. (2022), and Ye et al. (2022), respectively. (c) Assumed initial relative prestress ratio R , defined as the potential stress drop the full breakdown strength drop, constrained by fault geometry and geodetic coupling model (Zhao et al., 2022). (d) Modeled static stress drop.

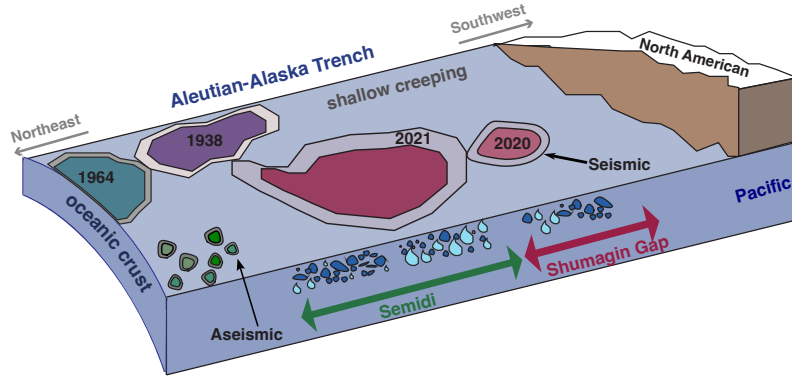


Figure 9. A diagram showing the tectonic setting and slip behaviors of the plate interface shear zone which change substantially along the fault between Semidi and Shumgain. The Pacific plate subducts beneath the North American plate. The solid contours represent seismic asperities that have hosted the coseismic ruptures of the 2020, 2021, and historical earthquakes. These seismic asperities are surrounded by various fault shear zone properties and shallower aseismic fault portions. The porosity and pore fluid change essentially along the strike, likely controlled by fault zone structure. The shallower and deeper parts of the seismogenic zone are accommodated by aseismic creeping